Nationaal Lucht- en Ruimtevaartlaboratorium
National Aerospace Laboratory NLR

NLR-TP-98139

Impact damage prediction and failure analysis of heavily loaded, blade-stiffened composite wing panels

J.F.M. Wiggenraad, X. Zhang* and G.A.O. Davies**

Nationaal Lucht- en Ruimtevaartlaboratorium

National Aerospace Laboratory NLR

NLR-TP-98139

Impact damage prediction and failure analysis of heavily loaded, blade-stiffened composite wing panels

J.F.M. Wiggenraad, X. Zhang* and G.A.O. Davies**

* *College of Aeronautics, Cranfield University*
** *Department of Aeronautics, Imperial College of Science, Technology and Medicine*

This report represents a publication submitted to the journal "Composite Structures".

Division:	Structures and Materials
Issued:	17 March 1998
Classification of title:	Unclassified

Contents

5 Tables
32 Figures

(42 pages in total)

IMPACT DAMAGE PREDICTION AND FAILURE ANALYSIS OF HEAVILY LOADED, BLADE-STIFFENED COMPOSITE WING PANELS

by

J F M Wiggenraad[a] , X Zhang[b] and G A O Davies[c]

[a] National Aerospace Laboratory NLR,
PO Box 153, 8300 AD Emmeloord, The Netherlands

[b] College of Aeronautics, Cranfield University,
Cranfield, Bedfordshire, MK43 0AL, United Kingdom

[c] Department of Aeronautics, Imperial College of Science,
Technology and Medicine, London, SW7 2BY, United Kingdom

Abstract

Within the framework of a European research programme to develop design methodology for the improvement of damage tolerance within composite materials, two heavily loaded, stiffened composite wing panels were designed, fabricated and tested. The panels were impacted at the vulnerable stiffener edges and the failure modes and mechanisms related to the infliction of *impact damage* and the subsequent *compression after impact* loading were determined. A capability to predict the occurrence of impact damage by finite element analysis was demonstrated and guidelines for the design of damage tolerant panels were established.

The laminate composition of two panel skins was quasi-isotropic. The test results were compared with test results obtained earlier for two similar panels with soft skins, i.e., panel skins with a low axial stiffness. The latter panels were shown to be more damage tolerant, which is accredited to the much smaller number of 90-degree plies present in the soft skins. The failure mode was found to be a three stage phenomenon: a load eccentricity is present from the start causing local bending near the damage area, impact delaminated sublaminates then buckle out of plane and eventually propagate leading to global bending and to overall instability and collapse. Delamination growth occurred mainly in the lateral direction along 90-degree ply interfaces, but remained within the C-scan damage area until the final unstable propagation. The stability of the damage configuration, and in particular of the sublaminates formed by the impact and the subsequent compression loading, seems to be the key with respect to the damage tolerance of heavily loaded, stiffened panels.

Keywords: impact damage, compression after impact, damage tolerance

1. INTRODUCTION

The use of advanced composite materials, and in particular of carbon fibre reinforced epoxy material, has become a common factor even in the conservative, economy driven design environment of today's civil aircraft. Empennage structures of Airbus and Boeing aircraft, as well as wing sections of the ATR-72 commuter aircraft are but the first examples of primary aircraft structures made of these materials, and there is more to come. Just like baseline material "aluminium", fibre reinforced composite materials are hampered by particular inherent weaknesses, which must be understood and accounted for in the design of a structure. Most manufacturing techniques for composite aircraft structures in use today, including the mature "prepreg/autoclave" technique, result in layered material build-ups. The dominant weakness of this material configuration is that impact damage, introduced accidentally during manufacture, operation or maintenance of the aircraft, may consist of delaminations between the layers in addition to matrix cracks and fibre fractures in the layers themselves. Delamination damage, when caused for instance by tools dropped at relatively low velocities, is difficult or even impossible to detect during visual inspections, but may increase in size under compression loading and lead to premature failure of the structure at loads below the design load. However, it is a requirement that aircraft structures, when containing invisible or Barely Visible Impact Damage (BVID), are able to carry the full ultimate design load. Hence, these structures must be designed to be damage tolerant.

The presence of delaminations affects the strength of composite aircraft structures in particular when these are subjected to in-plane compression loads. With increasing load, the thin sublaminates resulting from delaminations loose their stability, bend out of plane, and finally collapse when loaded in compression. Major aircraft structures which are loaded predominantly by compression are the upper skin panels of wings and horizontal stabilizers.

For an efficient design of composite aircraft structures and ultimately for their certification, the number of tests at all structural levels should be limited as far as possible. It is therefore essential that damage configurations resulting from low velocity impacts and the residual compression after impact (CAI) strength of

composite structures can be determined by numerical analysis. Such analysis methods must be based on a thorough understanding of the failure mechanisms involved, because the models to be developed should be sufficiently accurate to catch the essential phenomena of these mechanisms, while being simple enough to allow efficient computation. Moreover, a thorough understanding of the physics of the impact event and of the subsequent failure process under loading is needed for the development of guidelines for the design of damage tolerant structures. Obviously, it has to be admitted that numerical analysis procedures are sophisticated and computationally extensive to some extent. Therefore, these procedures should only be applied to suitable, i.e., damage tolerant candidate designs which do not have a fundamental weakness, so several failure modes may be involved in final collapse.

The present paper is aimed at developing these insights for the case of heavy, compression loaded, stiffened wing panels. The failure modes and mechanisms related to impact events and compression after impact loading are described, and a capability to predict the occurrence of impact damage by finite element analysis is demonstrated. Part of the work was performed by the authors within the framework of a European Research Programme [1] in which they co-operated. The first part of the paper describes the design of the panels, the second part compares and discusses the impact test and analysis results, and the final part of the paper describes the failure modes resulting from the compression after impact tests, and discusses the implications for damage tolerant design.

2. PANEL DESIGN

A well known damage tolerant design configuration is Boeing's concept for stiffened panels [2], consisting of "soft" skins (skins with low axial stiffness), discrete stiffeners (stiffener laminates separated from the skin laminates) and "padups" (laminated strips, interleaved within the skin underneath the stiffeners, named doublers), as shown in figure 1. This concept has since been applied to the V-22, while a further development, (the use of an improved material allowed the elimination of the doublers) was applied to the B-777 horizontal stabilizer [3]. This panel design concept was evaluated at NLR in the early nineties, and test results of two panel designs,

referred to as panels A and B, are used as baseline values for the present study. Configurations A and B had equal laminate compositions, but different stacking sequences in the doubler area: panel A had fewer and thicker doubler laminates interleaved in the skin, while panel B had more and thinner doubler laminates. The material properties and laminate stacking sequences of the two configurations are shown in tables 1-2.

Both panels were impacted underneath the stiffener edge with an energy of 100 J, and loaded in compression up to failure. Panel A failed unexpectedly at a higher load than panel B. To investigate the failure mechanism in more detail, a study was carried out using "structure relevant" (SR) specimens: small rectangular specimens which contained the same skin/doubler configuration as the panels [4-5]. This study indicated that the location of the major delaminations, formed by the impact event, played an important role in the residual strength. Moreover, it seemed that the location of these delaminations could be influenced by changing the stacking sequence.

Within the framework of the aforementioned European research programme [1] it was possible to further investigate this phenomenon, when two panels had to be designed and fabricated by NLR, for an impact test programme to be carried out by Imperial College. The panels were designed with a common laminate composition but with a different stacking sequence in the doubler area, and are referred to as panels C and D. These panels were designed for similar design loads and equal design strains as panels A and B. However, the design of panels C and D were constrained to have thinner (4 mm), quasi-isotropic skins as compared to the thicker (5.8 mm), soft skins of panels A and B, a constraint imposed by the objectives of the European research programme. Another constraint was the fact that the same tooling had to be used as was used earlier for panels A and B, for the fabrication of the skin panels with doublers for panels C and D, (the stiffeners were fabricated separately and were bonded afterwards to the skin panels), which governed the doubler geometry and stiffener pitch.

Within these constraints, panels C and D were designed for minimum weight with the use of panel optimization code PANOPT [6]. The cross section of the final design is shown in figure 1. The material properties, the laminate stacking sequences, the laminate composition and the overall axial stiffnesses of all four designs A-D are shown in tables 1-3. The design specifications and the resulting average panel

properties are shown in table 4. The much higher laminate stiffnesses and thinner skins of panels C and D compared to panels A and B (see table 3) resulted in a considerably higher overall stiffness and lower panel mass (see table 4). The penalty of the higher efficiency of panels C and D is the much higher stress (nominal strength) at which they have to operate when carrying the Design Ultimate Load (445 MPa versus 346 MPa for panels A and B).

Two 5-stiffener panels were fabricated according to designs C and D, and were mounted on three lateral rib simulation supports, two near the ends and one in the centre. The two panels were impacted at different locations and at different energy levels. The results of this impact test programme are described in the next section. After the impact test programme was completed, a smaller 3-stiffener panel, 500 mm wide and 450 mm long, was cut out of each the two 5-stiffener panels. The two panels, each containing one impact damage of approximately 100 J were subsequently loaded in compression up to failure. The results of this compression after impact test programme are described in section 4.

3. LOW VELOCITY IMPACT TESTS AND PREDICTION

3.1 Experimental

Panels C and D were impacted by an instrumented falling weight rig. Both the impactor mass and drop height were adjustable, which provided a wide range of incident energy of 8–200 J. The impact damage caused had different characteristics: from barely visible impact damage (BVID) to serious stiffener/skin debonding. This has enabled us to investigate the damage signature and damage tolerance of both panels.

a. Test Programme

Particular attention has been given to the influence of the structure's dynamic response and the different local resistance which is to be expected if the point of impact is mid-bay skin between stiffeners, over the stiffener edge, or precisely on the stiffener centre line

From the experience gained in testing and numerical simulation of the simple plates [7-8], it was apparent how local the damage areas were and how much the flexural resistance of the plates was degraded by fibre/matrix damage during the impact but hardly at all by the interior delamination. Thus we were able to conduct a whole series of impact tests at different sites on the panels, knowing that damage would not affect the behaviour elsewhere. (This turned out to be less true for the impacts over stiffeners at very high energy levels. Fortunately, these high energy tests were conducted at the end of the testing programme, and each panel only received one of such high energy impact.) Three impact locations were selected, i.e. mid-bay skin (denoted as site *M*), stiffener edge (site E), and stiffener centre line (site S), as indicated in figure 2. The impact energy was in the range of 6.5-50 J for the base skin laminate, 30-100 J for the stiffener edge, and 50-200 J for the stiffener centre line. The impact positions and incident energies for panel *C* are illustrated in figure 3. The impacts on panel D were very similar to Panel C.

All impacted locations were ultrasonically scanned by a portable device called *ANDSCAN*, which enabled damage to be inspected during the test schedule without removing the panel from the test rig. This advanced device provided a three-dimensional (3D) image of the detected damage area to show the depth of each delamination damage (see figure 5). The ultrasonic tests confirmed that the damage was sufficiently local to allow 16 tests per panel without interactions between individual damage zones. Microscopy section tests for some locations were also carried out when the testing programme was completed.

b. Test Results

Mid-bay skin between stiffeners (Site M)

The lowest energy of 8 J (panel *C*, site M1) did not cause any damage. Delamination started at the energy of 12 J (panel *C*, M2). As planned the maximum incident energy for the skin location was 50 J. Impact tests with almost the same sites and energies were conducted on panel D. C-scan maps showing progressive delamination with increasing energy are presented in figure 4. Although the interior delamination was in fact a series of overlapping ‘peanuts’, each in its local fibre direction, the envelope of these delaminations was almost circular in shape until the impact energy caused sufficient bending for matrix cracking to occur at the lower back face. This matrix

splitting was confined to a few layers and precipitated delamination at the adjacent interface. This separate form of delamination can be seen as the extra elongation in figures 4c and d, and were excluded in the measurement of the interior shear-driven delamination areas. Figure 5 presents the 3D image of test M2 previously shown in figure 4b by the conventional C-scan in terms of the total damage envelope. The ANDSCAN has the advantage of determining the depth of each delamination damage as figure 5 shows the damaged layers up to 2.86 mm in depth from the impact surface. The overlapping 'peanut' shapes are reasonably clear in this picture, but any damage will shield the area below in this *"time-of-flight"* mode. The extensive reflection below a depth of 2.86 mm are from the back surface of the plate and the edge of the inclined doubler face.

The test results of the skin impacts are plotted as damage area against peak impact force as well as damage versus incident energy in figure 6. The two panels are almost indistinguishable since they both have the same skin laminate. The force map is rather more revealing and shows that all impact sites have a sudden increase in damage at a critical load, whether the site is in a stiffened panel or in a small coupon specimen. This critical force can be predicted theoretically [8] to be 5440 N and is seen in the figure to be remarkably accurate. It's worth mentioning that there were four configurations in the tests of small coupons and large plates, which including two sizes, i.e. 125 x 75 and 200 x 200 mm and two boundary conditions, i.e. simply-supported and fully clamped. Figure 6a shows that the use of force makes the variations between coupons, plates and panels indistinguishable. This is good news if we wish to use coupon tests as a calibrator for real structures. The energy based map looks more chaotic. We can conclude therefore that a coupon test, followed by a finite element prediction for force history, would have predicted damage accurately in these panel skin impacts. This will be demonstrated in section 3.2. It remains to be seen whether this strategy works for impact close to another feature, like a support or stiffener.

Stiffener Edge Impact (Site E)

The edge positions were impacted from the flat side of the panel in the transition area of skin and doubler, i.e. the linear tapered area, as indicated in figure 2. Both panels

were impacted at four locations with increasing energies. The resulting damage areas were very similar for each panel at same energy levels despite the difference in the doubler sublaminates. Therefore, only the results of panel D are discussed here. The progressive damage development with increasing impact energy was monitored by C-scan. Firstly, at the lowest energy of all, 30 J at site E8 (figure 3), no significant delamination was found, but some surface damage within the first 1.1 mm from the impacted face was detected. The second test was over site E9 with 51 J. The damage area was about 270mm^2 as shown in figure 7a. At site E11 with 74 J the damage area was increased to 2800 mm^2, and finally at the highest energy of 104 J at site E12, the damage area was about 4000 mm^2, figure 7b. For the highest energy test, the back face matrix cracking was observed by eye extending to the basic skin. These C-scans also showed internal delamination of the same limited extent as for the basic skin tests, but the pattern is clearly more complex as we would expect in the tapered region where lamina were being phased out continuously from the stiffener flange to the basic skin.

The impact force histories in figure 8 for 51 J and 104 J show a characteristic shape which we recognise as evidence of damage. In an undamaged structure the response is virtually a sinusoidal fundamental mode signature, with occasionally a small higher harmonic component in complex configurations. The decay is identical to the rise. Any in-plane damage will lower the flexural stiffness, truncate the maximum force, and result in a longer decay. The effects are apparent in figure 8b.

In order to investigate the damage tolerance of the panels by CAI tests, a large 3-stringer part was selected and impacted over the stiffener edge (site E12) with the energy of approximately 100 J for both panels (fig. 3). Impact damage at this location is thought to be most critical to the compressive residual strength of the panel. The results of both panels were very similar as described above. The CAI tests are discussed in section 4c.

Stiffener Impact (Site S)

For impact over the more rigid 3-D region in the vicinity of a stiffener, the behaviour is likely to be very different from the impacts over the panel skin area. It wasn't immediately obvious what the consequences will be. For a given incident energy the peak force will clearly be higher for impact on a stiffer region, but then the smaller deflections may lead to lower strains.

To examine these conflicting effects, a series of tests was conducted over the stiffeners at the energy levels of 50 J, 100 J, 160 J and 200 J (fig. 3). The maximum resulting impact force at 200 J was approximately 35 kN. Two features emerged from the C-scanning, and were later confirmed by section micrographs. Firstly, there was again a local circular patch of delamination but this was confined to a small depth less than 1.5 mm below the impact surface. Secondly, at sufficiently high energy levels (beyond 100 J in this case) there was a massive debonding between the skin-doubler and stiffener flange which ran all the way to the nearest rib support. The C-scan images in figures 9a and 9b show this evidence. Thus, there were two different damage modes: local delamination in the skin-doubler (denoted as *A* in figure 9) and much more extensive debonding between the skin-doubler and stiffener (denoted as *B*).

The high-energy impact site was subsequently sectioned in order for optical microscopy to reveal further evidence of the failure mechanism. It was found that the impact surface was crushed under the very high force of 35 kN, forming a crater, pushing debris to either side. This extreme form of damage was largely a compressive crushing of both matrix and fibre, but confined to the top 2 or 3 laminas This very local damage needs not lead to serious reduction in strength. The sectioning test also confirmed the debonding failure detected by the *ANDSCAN* tests. Details can be found in [9]. The debonding between stiffener and skin-doubler was much more extensive, and potentially serious since it would reduce almost entirely the ability of the panel to resist compression. What appeared to be happening was that the doubler-stiffener region was behaving rather like a beam, loaded by a point force between two end supports (provided here by the metal ribs). If there was very little diffusion of the load to adjacent regions, the shear force responsible for the debonding would be constant between load point and supports and thus the debonding would progress all

the way to the support as sketched in figure 10. Similar tests were carried out on panel *C*. Again the tests confirmed the debonding at the incident energy levels beyond 100 J. The damage is no longer local. This phenomenon will be simulated numerically in section 3.2.

c. Discussion of test results

The panels turned out to be more damage tolerant than expected, in the stiffener region, as the incident energy went to 100 J for stiffener edges and 200 J over the stiffener web. The damage threshold for impact over the stiffener was much higher than for impact elsewhere, needing more than 100 J to cause significant damages. The nature of the damage also changed dramatically from a local delamination to an extensive debonding failure all the way to the panel rib support. The 200 J impact over the stiffener might be too high to be realistic. For example, the U.S. Mil. Spec. calls for 100 ft-lb (≈140 J) to represent the energy threshold [10]. However, the 100J impact over the stiffener in this study still caused significant debonding failure extending some 180 mm, which would reduce the CAI strength considerably.

3.2 Numerical modelling of impact damage

Damage tolerance testing of real structures is expensive and design is problematic. We therefore simulated the impact tests by finite element method. Selected impact tests were simulated using an explicit non-linear structural dynamics finite element code, FE77 [11]. Plate elements were used in this study. The elements were standard 8-noded *Mindlin* quadrilaterals which incorporate the important through-thickness shear flexibility. To model laminated composite materials FE77 requires only the basic laminar properties and the stacking sequence to be specified. It then assembles the stiffness and mass matrices of any composite structure. The code can model large deformations, and update the stiffness due to any membrane stretching induced when the maximum deflection exceeds the plate's thickness as often happens. It will also model the loss in flexural stiffness as fibres fail during impact: this is important since the impact force will then be attenuated. The composite damage model implemented in the *FE77* code was the Chang-Chang's failure criteria [13–14], permitting the simulation of three in-plane failure mechanism, i.e. fibre breakage, matrix cracking due to tension and matrix failure in compression, in any layer of the laminate at any

instant in the impact event simulation. Whenever damage occurred, the elastic properties of the element involved were degraded and the stiffness of the structure was updated to reflect this change in the next time step. Details are given in [8]. Through these calculations, the initiation and propagation of the in-plane damage was simulated.

The simplified finite element model for impact simulation was a 2-stringer substructure. Connections between the base skin, skin doubler, stiffener flange and stiffener webs were simulated by using constant thickness plate elements, but allowing for offsets from the base plate, as illustrated in figure 11. FE77 has the ability to 'bond' the plate assemblies together with rigid links. The final mesh and the extent of panel chosen in figure 12 was found by refinement in [12].

a. Skin impact simulation

For the mid-bay skin positions the FE model is shown in figure 12, which is a 2-stringer sub-structure and also cut short between the two rib supports. The boundaries of the substructure were modelled as simply supported edges. For the lowest energy case (6.4J) where no damage was found, the predicted impact force and displacement histories agreed extremely well with the test as shown in figure 13. The dynamic response was almost fundamental but a higher frequency mode was also clearly present. This example demonstrates that the *FE* model works very well.

Figure 14 shows a higher energy impact (26 J). The shape of the recorded impact force history and the *C*-scan image revealed that considerable flexural degradation took place. Thus degrading the FE model was necessary to bring the force history in line with the test result as shown in figure14a. Both the predicted and experimentally recorded maximum impact forces were close to the value of 6800 N. The measured maximum displacement was approximately 6 mm as shown in figure 14b, about 1.5 times of the panel skin thickness, thus the non-linear analysis was necessary. The predicted in-plane damage area of 1230 mm^2, figure 14c, agreed very well with the C-scan measured 1100 mm^2. The actual damage is essentially multi-layer delamination damages as shown in figure 5. The C-scan detected damage area, 1100 m^2, is the envelope of total delamination damages. This is a simple measure of the damage area contributed by all layers of the laminate. Although the FE model uses 2-D plate elements, each layer's properties have been assembled in the plate stiffness matrix.

During the FE analysis, the degradation routine will check each layer's stresses and degrade the material's properties if any fibre/material stresses in the layer exceed the laminar strength values. The stiffeness of the structures is then updated to reflect this change in the next time step.

Stiffener impact simulation

For the stiffener impact tests we concentrated on predicting the debonding failure between the stiffener flange and skin. The physical and qualitative explanation for the debonding failure was reasonably clear. As mentioned the very high induced forces attempted to follow the stiffest path to the rib supports, i.e. along the stiffener, with little incentive to diffuse sideways to adjacent stiffeners, unlike plate impact where the shear stress decays rapidly like $\frac{1}{r}$.

In the *FE* model, the mesh was refined near the impact site to capture the stresses more accurately. The important transverse shear, τ_{xz}, was modelled as constant through the depth of the plate-stiffener flange therefore the maximum values could be up to 50 per cent higher. The flange/blade intersection was really a local stress concentration area but the FE model should give an estimate of the peak shears at the middle of the blade-angle/skin-doubler intersection, before they die away to zero at the edge of the stiffener flanges. Figure 15a shows the local sections used to display stresses along the stiffener length (*A–A*) and across section *B–B*. Results for impact site *S5* (panel *D*) with 203 J are presented which is equidistant from the rib supports so that stresses are symmetrical about *C–C*. Figure 15b shows the distribution of stresses at the stiffener flange and blade intersection (along *A–A*). The peak stress of 88 MPa occurred very close to the impact site and then decreased to an almost constant value of 40 MPa, all the way to the support. This confirmed where the shear stress, in the skin beyond the flange edge 53 mm, has become very small there was no diffusion to adjacent panels and the variation of stress across section B−B also confirms this (fig. 15c). The peak shear of 88 MPa should be 50% higher for the following reason. The *Mindlin* plate elements only give constant interlaminar shear stresses through the thickness, but the real shear stress distribution through the

thickness is parabolic. Thus to use the known interlaminar strength of 85 MPa as a criterion for debonding (or delamination) was a reasonable strategy. In fact there was a rapid decay to 40 *MPa* which suggests that the very local peak force initiated an unstable fracture. However the *FE* analysis does give a very credible confirmation of the expected internal stress field, and this stress distribution can be used for explaining the debonding failure at higher incident energies. Further work is necessary to embed a much finer 3-D mesh in the stiffener-flange area.

c. Discussion

All other numerical predictions of impact response and damage gave consistently good results and this means that the *FE* code and the panel models are adequate and reliable. The finite element models employed are quite easy to build and run times vary from a few hours (for stiffer region with linear deformation) to about 10 hours (with large deflection and damage degradation). For example, the computing time for the mid-bay site impact (*26J, M3*, 3.6 millisecond impact event) simulation was about 11 hours on a 1993 IBM RS 6000 workstation. Current models would reduce this to less than 30 mins.

4. FAILURE ANALYSIS

a. Failure mechanisms of panels A and B

During the late eighties and the early nineties, several series of composite stiffened wing panels were fabricated and tested by NLR to support a composite wing box technology programme of Fokker. Baseline panels A and B (with 100 J impact damage under the stiffener edge) were among these panels, and their load versus end-shortening curves are shown in figs 16 & 17. From these curves it is apparent that the failure modes were stable over quite a loading range. Audible damage growth was perceived first at strain levels of approximately 0.0045, and even during the final loading stage, several load drops were experienced after which reloading was possible before the panels collapsed. However, the failure loads of the two panels were quite different, at nominal failure strains of 0.0059 for panel A and 0.0047 for panel B (table 5). The nominal failure strain is defined as failure load divided by panel stiffness at zero load. Actual failure strains, which incorporate the apparent stiffness nonlinearity of the panels and the local failure phenomena that occurred, were higher

at 0.0066 and 0.0058.

To find an explanation for the different failure loads of the two panels, which were considered to be different only with respect to the fabrication effort that was involved but equivalent in strength, photographs were made of lateral cross sections near the fracture lines, shown in figures 18 and 19. The photographs show the skin/doubler section where the impact had taken place, with the stiffener missing. Apparently, the failure mechanism consisted of the subsequent buckling of several delaminated sublaminates, followed by the crippling of the skin and the collapse of the separated stiffeners. It can also be seen that the load drops in the load versus end-shortening curves (Fig. 18-19) may well have corresponded with the subsequent buckling of the delaminated sublaminates. Figure 18 shows that panel A had developed two thick sublaminates, while panel B (figure 19) had developed at least four thinner sublaminates. It was thought that the difference in thickness of the respective doubler laminates, 6 plies for panel A and 3 plies for panel B, was the reason for the different panel strength: thicker sublaminates buckle at higher loads than thinner sublaminates. The designs for panels C and D were subsequently defined on the basis of this conclusion: panel C with 6-ply doubler laminates and panel D with 3-ply doubler laminates. Note that panels C and D were made with thinner material plies than panels A and B (see table 1).

b. Failure mechanisms of SR specimens

In parallel with the design, fabrication and impact testing of panels C and D, a preliminary investigation was carried out at NLR to determine if the failure mechanisms that were observed in stiffened panels could be repeated in smaller and cheaper, "structure relevant" (SR) specimens: rectangular specimens with the same skin/doubler configuration as the stiffened panels, and supported by a suitably configured anti-buckling guide [4-5]. This study focused on panel configuration C. During fabrication, artificial delaminations were induced by inserting two circular bronze foils (of 30 µm thickness and 60 mm diameter) in the ramp area on top of selected doubler laminates (fig. 20): either on the first and second doubler laminates (interfaces 10/11 and 20/21, see table 2) or on the second and third doubler laminates (interfaces 20/21 and 30/31).

When loaded in compression, stable delamination buckling and growth was observed before collapse for the first configuration (with the foils placed nearer to the surface). The delaminations of the second configuration (with the foils placed deeper inside the laminate) had not grown when the specimen fractured, which occurred at a location away from the artificial delaminations, but at approximately the same strain level (0.0060) as the first configuration. A similar specimen, impacted with 36 J at the location where the artificial delaminations were already present, also collapsed without stable damage growth. However, in this case strain gauges and an LVDT located at the impact site indicated a distinct nonlinear strain increase before failure, which was not observed elsewhere on the specimen.

More importantly, the post-mortem photographs of lateral cross sections taken near the fraction lines of the specimens, indicated that the ply interfaces where the artificial delaminations had been placed were not the interfaces along which the delaminations propagated under loading. Instead, the delaminations jumped immediately to the adjacent 90-degree ply interfaces: 7/8 and 17/18 for the first configuration (fig. 21). So in fact, the ply interfaces where impact induced delaminations propagate under loading are not only determined by the stability of the 0-degree dominated doubler laminates, but also by the presence and location of the 90-degree plies. The same phenomenon is visible in figures 18 and 19 for panels A and B: most of the major delaminations are seen to have propagated along the 90-degree plies, which are the white lines in the photographs.

c. Failure mechanisms of panels C and D

Upon completion of the impact damage test programme describedin chapter 3, the two 3-stiffener panels C and D, each containing one 100 J impact damage underneath the stiffener edge, were cut from the original 5-stiffener panels as shown in figure 3. The C-scan image of the damage in panel D is shown in figure 7b. The characteristic apple shape, typical for this panel design concept [15], with the larger bottom part located in the stiff doubler region touching the centre of the stiffener, the top part extending slightly into the soft skin area. The panels were instrumented and tested by Imperial College according to the test plan defined earlier by NLR. The panel testing machine

is a large hyperstiff facility which can be arrested when the composite structures show signs of imminent failure. The instrumentation consisted of strain gauges (see Fig. 22), LVDT's to record the end-shortening, and a video camera was used to see if any stable damage growth, related to the buckling of sublaminates, could be observed during the test at the flat, impacted side of the panel. The instrumentation was quite extensive, because it was intended to study local phenomena for a more precise deduction of the failure mechanisms: bending or buckling of the skin, bending of the stiffeners, load redistribution, lateral delamination growth at the impacted flat side of the panel, and damage growth at the stiffened back side of the panel.

Panel C was tested first, up to a load of 1710 kN, when a loud cracking sound was heard. The specimen was unloaded, but no extension of the C-scan damage area was observed, using ANDSCAN. The panel was loaded again, up to a load of 1780 kN when it failed at an unexpectedly low load level, corresponding to an overall strain level of only 0.0036. After failure, the load dropped back to 1250 kN, which was carried entirely by the stiffeners which were still intact. The failure load corresponds to a running load of 3560 N/mm, while the design load was 4500 N/mm. It had not been the intention to fail the panel during the test, but to stop the load in time, in order to determine the damage configuration after a certain amount of damage growth had taken place, and so to establish the failure mechanism. Subsequently, panel D was loaded three times, each time up to a higher load, to make sure that the panel would not fail. During the first test a load of 1100 kN was reached, during the second test a load of almost 1500 kN was reached, and during the third test, a maximum load of 1660 kN was reached, still without failure. The test results are shown in table 5.

The final collapse of panel C was accompanied by the unstable buckling of a sublaminate at the damage site, as observed with the video camera. In figure 23 this phenomenon is shown on three subsequent photographs taken by the video camera at 25 images per second, hence, the images are separated by 0.04 seconds. The first shape of the buckle is a peanut shape with the major axis in the longitudinal direction. In the second photograph, the upper part of the buckle has developed two lobes, one on either side in the lateral direction. The third photograph shows total fracture upon the complete extension of the lobes to the sides of the panel. The shape of the buckled delamination was not the often assumed ellipse growing in a self similar pattern. It is

also not obvious that it is the buckling of the outer sublaminate that initiated the final failure. It is more likely that one or more 0-degree ply stacks collapsed due to out of plane bending, one part sliding past the other, thereby prying off the outer 45-degree plies in a non-symmetric manner. Such behaviour was observed in more detail [16] on a similar, 0-degree dominated laminate. Figure 24 shows a photograph of a cross section of the laminate of Ref. 16, taken in the longitudinal (loading) direction. The white layers are 0-degree plies in this photograph.

A post-mortem view of panel C after it failed in compression is shown in figure 25. The cross section is taken close to the fracture line. It is clear that many thin sublaminates with a low buckling resistance were formed by the delaminations, all of which followed the 90-degree plies (which are the white lines in the photograph). The fact that panel C had relatively thick doubler laminates did not result in a high failure load. Instead, the presence of the many 90-degree layers (19% of all plies in the doubler region were 90-degree plies, versus only 10% for panels A and B), and their dispersal (see table 2) resulted in many thin 3-ply and 5-ply sublaminates, each containing no more than three 0-degree plies, which could buckle out at relatively low loads. Instead, panel D with thinner doubler laminates might have failed at a higher load. Its 90-degree plies were grouped in pairs, which resulted in a doubler region containing only 11% 90-degree ply interfaces (see table 2). The 8-ply sublaminates, formed by the major delaminations which again followed the 90-degree plies, were much thicker than those of panel C. Each sublaminate contained six 0-degree plies and would have buckled at a much higher load. A post-mortem view of panel D is shown in figure 26a. Panel D had been loaded in compression, but not up to failure, and no growth of the C-scan damage area was detected afterwards. The panel was dissected through the impact site. The location of the larger impact induced delaminations of panel D are more clearly shown in figure 26b, on a photograph taken under u.v. light, in which the delaminations, impregnated with a penetrating fluid, show up as white lines. Comparison of figures 26a and 26b shows that the large delaminations are adjacent to the 90-degree plies.

d. Essential failure characteristics

In figures 27-32 the test data for panels C and D are compared. The data for panel C were recorded during the second and final test run up to failure, for panel D the data were recorded during the third and last test run, which was stopped before failure. The load versus end-shortening curves are shown in figure 27. The curve for panel C became non-linear during the final loading stage as the result of the propagation of the impact damage, as discussed later. The curve for panel D remained linear, but the test was stopped at the load level where the curve of panel C became non-linear. Figure 28 shows the absence of any significant bending or buckling of the skin away from the impact damage location. Figure 29 shows for both panels that from the onset of loading, considerable bending took place of the centre stiffener in the direction towards the flat, impacted side of the panel, while the adjacent stiffener remained straight all the way through. Load (strain) redistribution is shown in figure 30. Apparently, the outer stiffener away from the impact damage (strain gauge #1) escapes some of the loading, which occurred from the onset of loading. Figure 31 shows the strain distribution in the damaged region. Strain gauge 7, located on top of the impact site, escapes the loading already in the lower loading range. This happened earlier and more significantly for panel C, but it should be kept in mind that this behaviour reflects the deformation of the outer delaminated sublaminate. Strain gauge 7 shows that the surface is undergoing tensile relief, that is, a sublaminate near the impact damage is buckling at an applied mean strain less than 1000 $\mu\varepsilon$. In the case of panel C, this sublaminate is probably only two plies thick (the first 90-degree ply is only three plies deep), while in case of panel D, this sublaminate is probably four plies thick.

A closer view of the behaviour of the damaged region is shown in figure 32. Strain gauges 7 and 8 are located on top of the damaged site, in the longitudinal and lateral panel directions, respectively. Figure 32a shows that the damage in panel C propagates extensively during the last stable load steps, which are the load steps corresponding to the non-linear part of the load versus end-shortening curve in figure 27a, but before the unstable buckling shown in figure 23 took place. In particular, the lateral strain gauge 8 shows a large change in strain at hardly any change in load. This effect is shown even more clearly in figure 32b, in which the loading and unloading

curves are shown for strain gauges 7 and 8 for all three test runs of panel D. The longitudinal strain gauge 7 indicates a reversible bending of the outer sublaminate, but lateral strain gauge 8 shows a non-reversible strain increase during the second and third test run, indicating damage growth in the lateral direction.

In conclusion, three phases can be distinguished during the loading of panels C and D, each of which are governed by the presence of impact damage. From the start of loading, a load eccentricity is present, which causes the stiffener closest to the damage to bend increasingly. At a certain stage, the outer sublaminate in the damaged area bends out, and damage develops in the lateral direction without enlarging the C-scan area. In the final stage, which was not reached in case of panel D, the load eccentricity has become so large that a global non-linearity occurs, which is clearly visible in the load versus end-shortening curve. This non-linear behaviour corresponds to a severe bending backwards at the damaged area, which is reflected in the strain reversal towards compression of the sublaminate in the damaged area (strain gauge 7), as well as in a sudden increase of the bending of the 9 mm thick skin/stiffener flange region nearby (strain gauges 6/17).

Panels A and B were not instrumented as extensively as panels C and D. The load versus end-shortening curves were also observed to become non-linear, but during the final loading stage, panels A and B survived the sequential buckling of several sublaminates before the panels collapsed. It is thought that the laminate composition (a limited number of 90-degree plies), the stacking sequence (thick sublaminates between 90-degree plies) and also the overall skin thickness (5.6 mm for panels A and B versus 4 mm for panels C and D) are the key factors to achieve a high compression after impact strength, i.e., for the design of a damage tolerant panel.

As yet, it has not been tried to determine the failure strength of panels A-D by numerical analysis. The experimental results presented here were intended to provide insight into the essential failure characteristics that must be captured by the analysis. In particular, it should be pursued to model the decreasing stability of the C-scan damage area itself under increased loading, in addition to the "classical" problem of delamination growth.

5. CONCLUSIONS

Within the framework of a European research programme to develop design methodology for the improvement of damage tolerance within composite materials, two heavily loaded, stiffened composite wing panels were designed, fabricated and tested. The failure modes and mechanisms related to the infliction of impact damage and the subsequent compression after impact loading were determined. A capability to predict the occurrence of impact damage by finite element analysis was demonstrated and guidelines for the design of damage tolerant panels were established.

The use of simple finite element plate models, to predict impact force histories and in-plane damage, worked well and it was shown that in-plane degradation is needed for high incident energy. The success of the predictions, which avoid using 3-D FE analysis, has been validated by experimental tests on these stiffened panels. An order of magnitude increase in the power of workstations is needed to make this FE simulation a design tool.

The failure mode of two panel designs were compared to the failure modes of two alternative panels. The difference between the two series of panels was the laminate composition of the panel skins: quasi-isotropic skins versus soft skins, i.e., skins with a low axial stiffness. The latter panels were shown to be more damage tolerant, which was accredited to the much smaller number of 90-degree plies in the soft skins.

The failure mode was found to be a three stage phenomenon: (a) a load eccentricity is present from the start causing local bending near the damaged area; (b) delaminated sublaminates bend out of plane; (c) unstable propagation of the sublaminate causes global bending and thence overall instability and collapse. Delamination growth occurred mainly in the lateral direction along 90-degree ply interfaces, but remained within the C-scan damage area until the final, unstable loading stage.

It should be pursued to model the stability of the damage configuration, and in particular of the sublaminates formed by the impact, in order to determine the compression after impact strength by numerical analysis of the heavy loaded, stiffened panels considered in the present study. The stability of these sublaminates is governed by their thickness, laminate composition and location within the laminate.

6. ACKNOWLEDGEMENTS

The authors would like to acknowledge the support of the European Commission (under Brite Euram 3159) and the programme managers British Aerospace.

7. REFERENCES

1. Frame, C. S., "Design Methodology for the Improvement of Damage Tolerance within Composite Materials"–Brite Euram Contract BREU/0276/C, 1993.

2. McCarty, J.W. and Roesseler, W.G., "Durability and Damage Tolerance of Large Composite Primary Aircraft Structure", NASA CR-003767, 1984.

3. Miller, A.G., Lovell, D.T. and Seferis, J.C., "The Evolution of an Aerospace Material: Influence of Design, Manufacturing and In-Service Performance", *Composite Structures*, Vol. 27, Nos 1 & 2, 1994.

4. Labonté, S. and Wiggenraad, J.F.M., 'Development of a Structure Relevant Specimen for Damage Tolerance Studies', *9th International Conference on Composite Materials*, Madrid, Spain, 1993.

5. Labonté, S. and Wiggenraad, J.F.M., "A Damage Tolerance Study Conducted with Structure Relevant Specimens", NLR TP 93067 U, 1993.

6. Arendsen, P, Thuis, H G S J and Wiggenraad, J.F.M., "Optimization of composite stiffened panels with postbuckling constraints", *4th Int. Conference on Computer Aided Design in Composite Material Technology (CADCOMP 94),* Southampton, UK, 1994.

\

7. Davies, G.A.O., Zhang, X. and Edlund, A., "Predicting damage in composite aircraft

structures due to low velocity impact", *Aerotech'94*, Birmingham, U.K., Jan. 1994.

8. Davies, G.A.O. and Zhang, X., "Impact damage prediction in carbon composite structures", *Int J. Impact Engineering*, **16**(1995),149-170.

9. Zhang, X and Davies, G.A.O., "Low velocity impact damage in stiffened CFRP panels", Brite-Euram 3159, Final Report, Aeronautics Dept, Imperial College, U.K., 1993.

10. Sierakowski, R., "Towards a damage tolerance philosophy for composite materials", *9th International Conference on Composite Materials*, Madrid, Spain, 1993, 15-21.

11. D. Hitchings, FE77 general purpose modular finite element system for static and dynamic, linear and non-linear analysis, Dept Aeronautics, Imperial College.

12. Zhang, X. and Davies, G.A.O., "Design Methodology for Improving Damage Tolerance in Composite Structures: Task 2.0 Finite element modelling of the damage mechanics", Brite-Euram 3159, 4th Report, Aeronautics Dept, Imperial College, London, U.K., 1993.

13. Chang, F K and Chang, K Y, "A progressive damage model for laminated composites containing stress concentrations", *J. Composite Materials*, **21** (1987), 834-855.

14. Choi, H Y and Chang, F K, "A model for predicting damage in graphite/epoxy laminated composites resulting from low-velocity point impact", *J. Composite* Ubels, L.C. and Wiggenraad, J.F.M., "A Method to Apply Structure Relevant Impact *Materials*, **26** (1992), 2134-2169.

15. Damage to Structure Relevant Specimens for Damage Tolerance Studies", *10th International Conference on Composite Materials*, Whistler, Canada, 1995, also in *Applied Composite Materials*, **4**, 1997.

16. Wiggenraad, J.F.M. and Ubels, L.C., "Impact Damage and Failure Mechanisms in

Structure Relevant Composite Specimens", 11th International Conference on Composite Materials, Gold Coast, Australia, 1997.

Tabel 1 Unidirectional ply properties of Fibredux HTA/6376

	Panels A and B	Panels C and D
Ply thickness	0.181 mm	0.125 mm
Ex, longitudinal stiffnes	124.0	135.0 Gpa
Ey, lateral stiffness	9.0	9.5 Gpa
υxy, Poisson´s ratio	0.3	0.3
Gxy, in-plne shear modulus	5.1	5.8

Table 2 Combined skin and doubler stacking sequences

Panel Number	Laminate stacking sequence
A	[(0/45/-45/90-45/45){0_5/90}(-45/45/45/-45){0_6}, (-45/45/90/45/-45/0){0_4}(0/45/-45/90/-45/45), {0_6}(-45/45/45/-45){90/0_5}(-45-45-90-45/-45/0)]
B	[(0/45/-45/0){90/0}(45/-45){0_3},(45/-45), {0_3}(0/45/90-45){0_3}(45/-45/45/-45){0_3}(45/90/-45), {0_3}(45/-45){0_3}(45/90/-45){0_3}(45/-45){90/0}(0/45/-45-0)]
C	[[(45/-45/90/0){0_2/90/0_3}]$_3$, [(45/-45/90/0){0_4}(0/90/-45/45)], [{0_3/90/0_2}(0/90/-45/45)]$_3$]
D	[[(45/-45){0_2/90})90/0){0_3}]$_3$, [(45/-45){0_2}(90/0_2/90){0_2}(-45/45)], [{0_3}(0/90){90/0_2}(-45/45)]$_3$]

Note: (laminates) are continuous skin sub-laminates
{laminates} are doubler sub-laminates

Table 3 Laminate properties

Panel number	Panel laminate	Laminate composition (plies)	Laminate composition (%)	Thickness (mm)	Youngs modulus (Gpa)
A and B	skin skin + doubler half stiffener	[4/24/4] [30/24/6] [16/8/2]	[13/75/13] [50/40/10] [62/31/8]	5.79 10.86 4.706	35.4 73.7 84.7
C and D	skin skin + doubler half stiffener	[8/16/8] [42/16/14] [28/8/2]	[25/50/25] [58/22/19] [74/21/5]	4.0 9.0 4.75	52.9 88.7 106.3

Note: Panels A, B ply thickness – 0.181 mm, panels C, D ply thickness = 0.125 mm.

Table 4 Panel design specifications and properties

Design specifications				Resulting properties			
Panel number	Design load (N/mm)	Design failure strain	Design length (mm)	Average thickness (mm)	Average stiffness (GPa)	Nominal strength (MPa)	Panel mass (kg/m^2)
A,B	4300	0.0050	n.a.	12.43	69.2	346	19.10
C,D	4500	0.0050	550	10.53	89.0	445	16.19

Specimen geometry: 3-stiifener panel, width 500 mm, length 450 mm
Nominal strength = average stiffness x design failure strain

Tabel 5 Impact damage and failure data

Panel number	Impact energy (J)	C-scan area (mm^2)	Failure load (kN)	Nominal failure load (kN)	Actual failure strain (μ)	Nominal failure strain (μ)	Failure stress (Mpa)
A	100	2400	2630	2231	0.0066	0.0059	408
B	100	3900	2100	2231	0.0058	0.0047	325
C	103	4000	1780	2432	0.0035	0.0036	326
D	104	4000	>1660	2423	>0.0033	n.a.	n.a.

Note:
- A semi-spherical indentor was used with 0.5 inch radius.
- Impactor mass of panels A,B: 5.09 kg, of panels C,D: 16 kg.
- Nominal failure load accounts for the smaller end zones = 0.005 x ΣEA based on the actual panel dimensions.

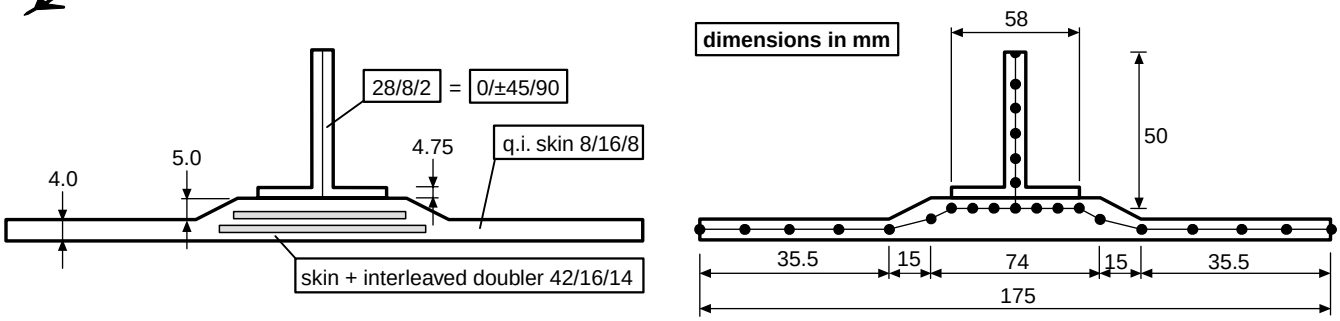

a) Thickness and lay-up of optimized configuration (one stiffener pitch)

b) PANOPT model and geometry of optimized configuration

Fig. 1 Panel design and configuration of panels C and D

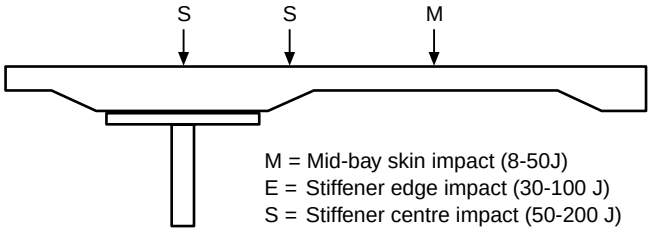

Fig. 2 Impact locations

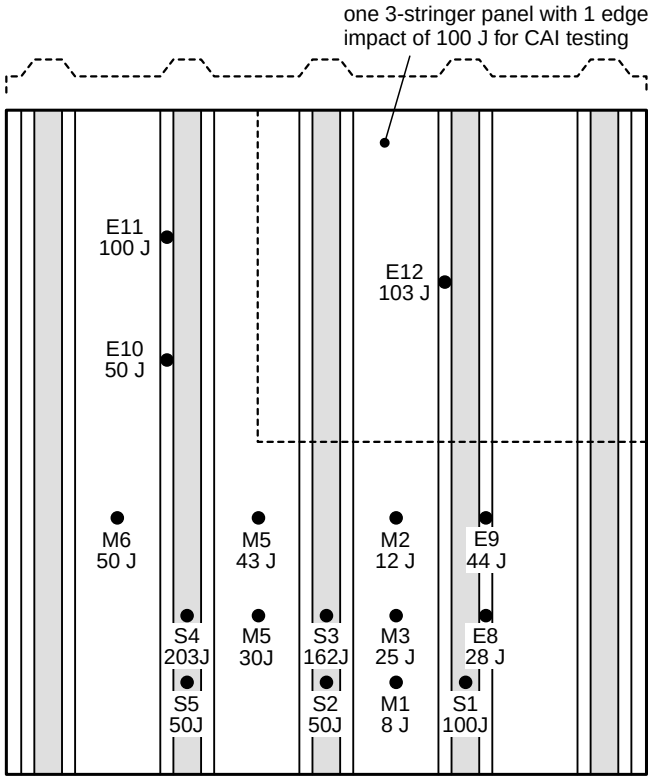

Fig. 3 Impact sites and incident energy levels for panel C

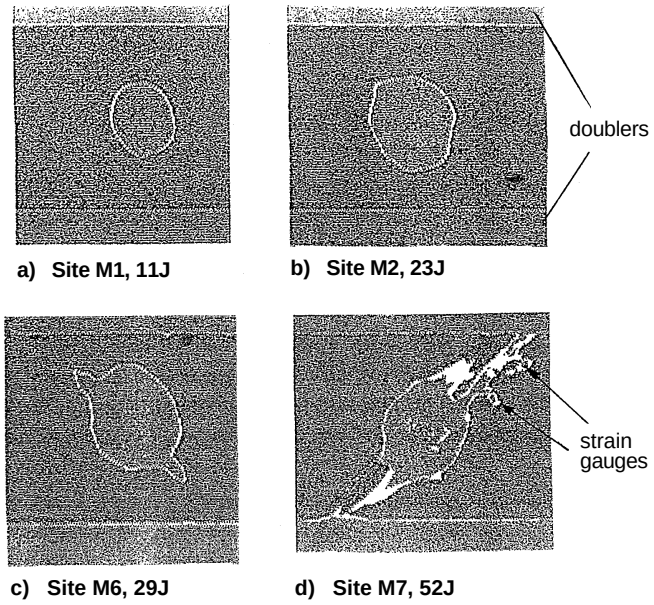

Fig. 4 C-scan pictures for impact tests on base skin of panel D

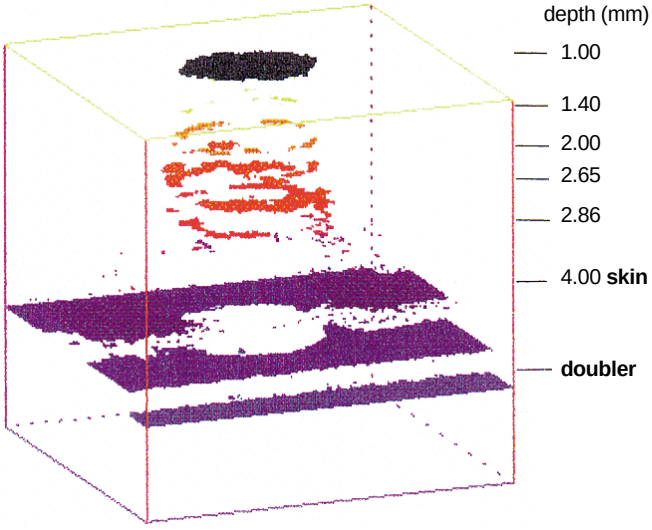

Fig. 5 3D Andscan test for impact on site M2, 23 J (panel D)

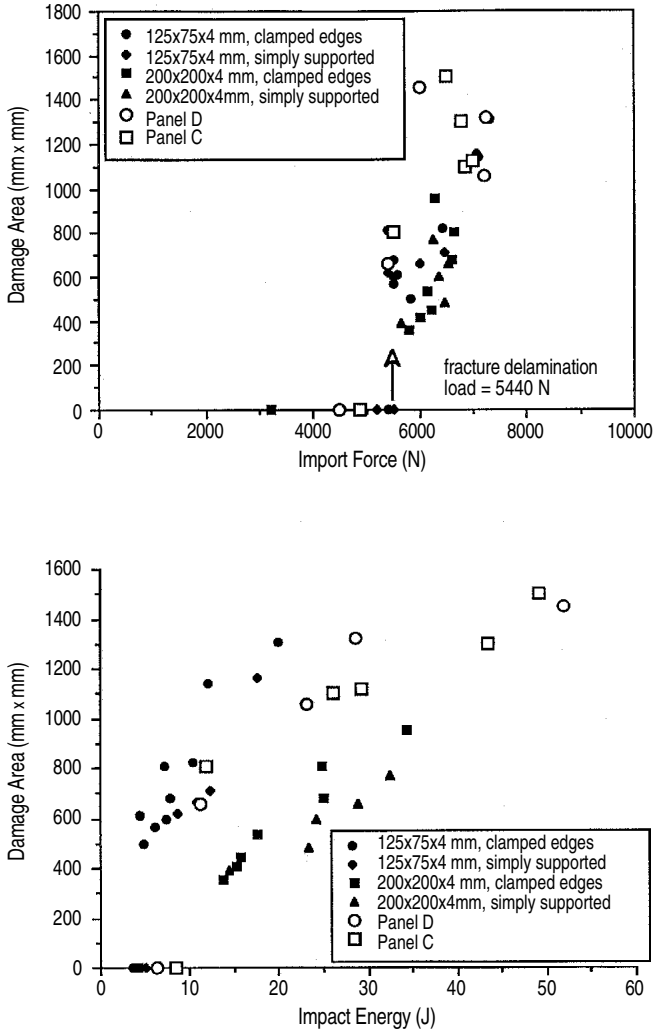

Fig. 6 Damage maps of coupons and panel skins together (laminate thickness = 4 mm)

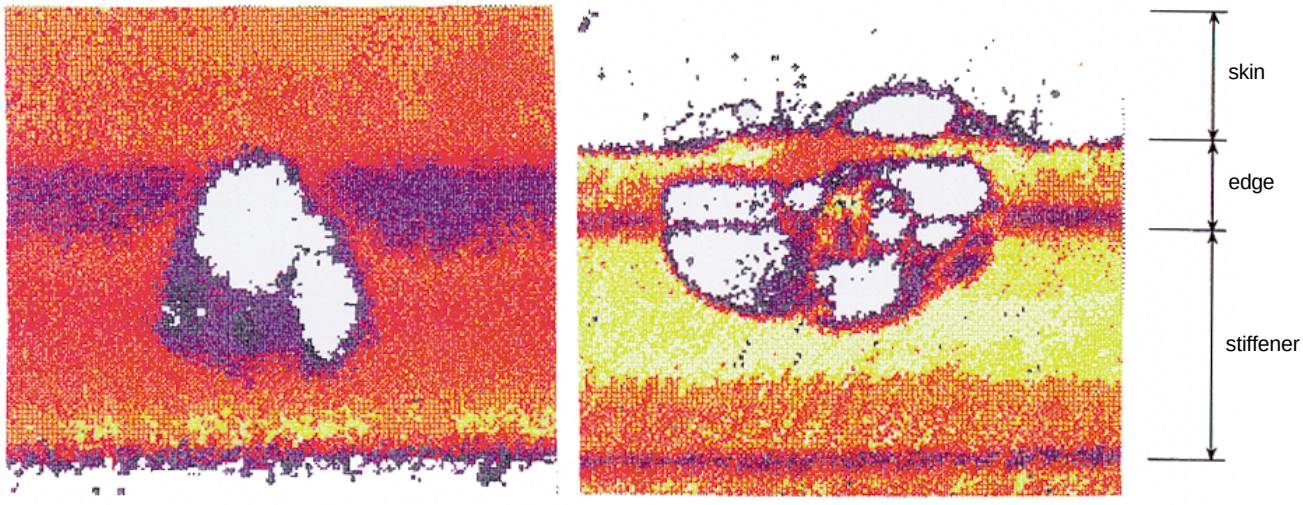

a) Site E9, 51 J **b) Site E12, 104 J**

Fig. 7 C-scan maps showing progressive damage for edge impact tests (panel D)

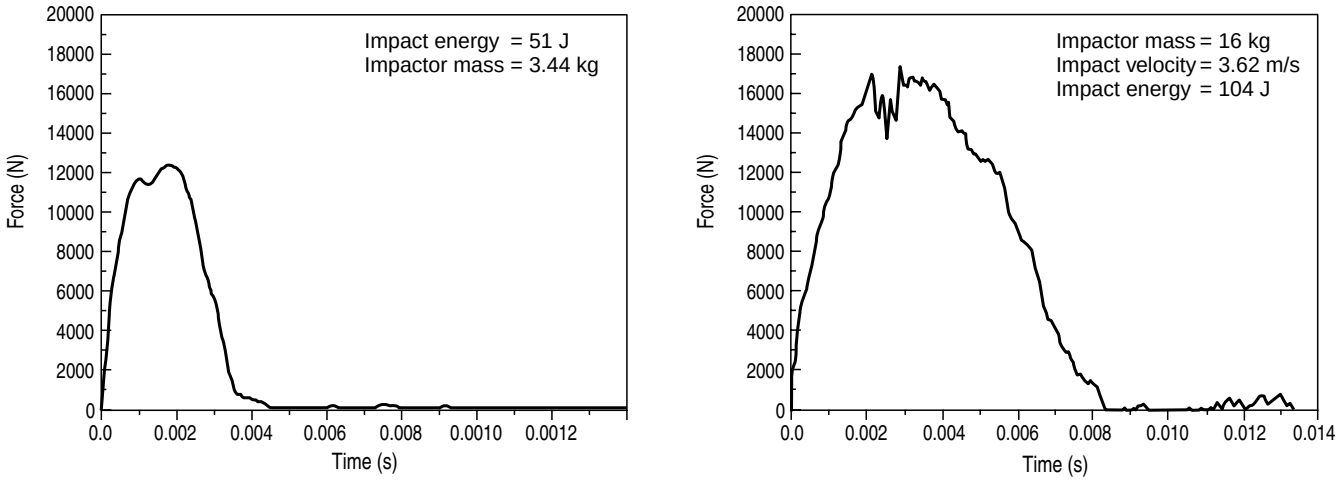

a) Site E9, 51 J **b) Site E12, 104 J**

Fig. 8 Impact force-time histories for edge impact of panel D

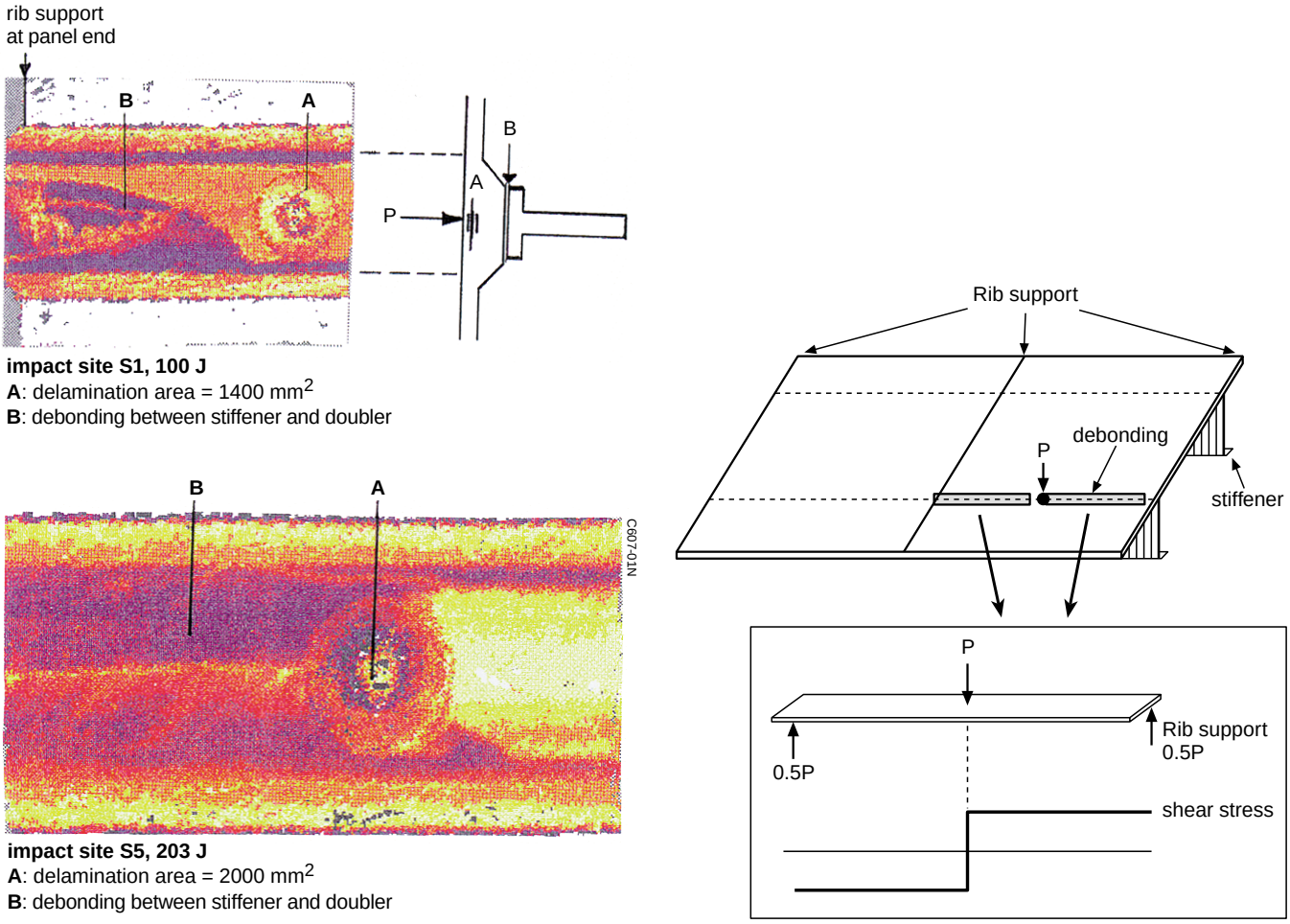

Fig. 9 Andscan images for impact tests over stiffener centre (panel D)

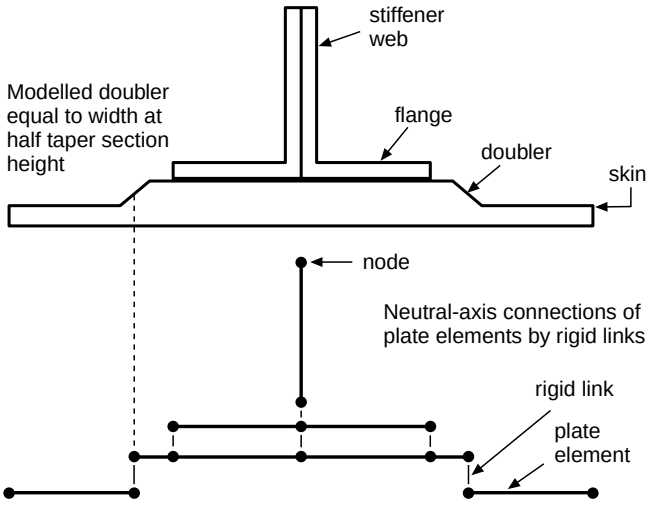

Fig. 11 Finite element model of portion of stiffened panel

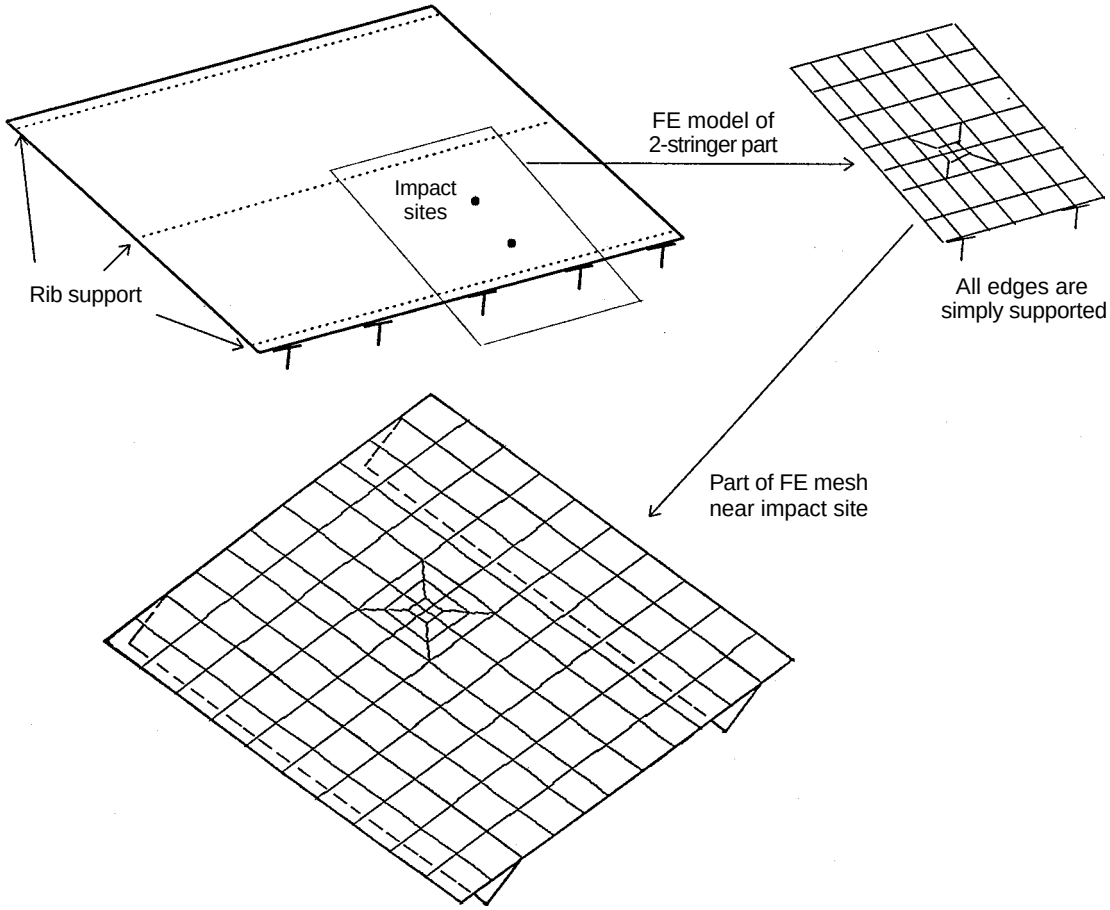

Fig. 12 Finite element model for skin impact simulation

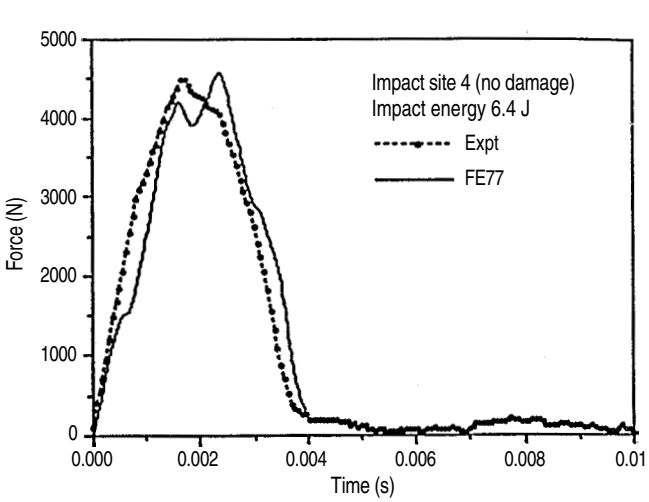

a) Impact force history

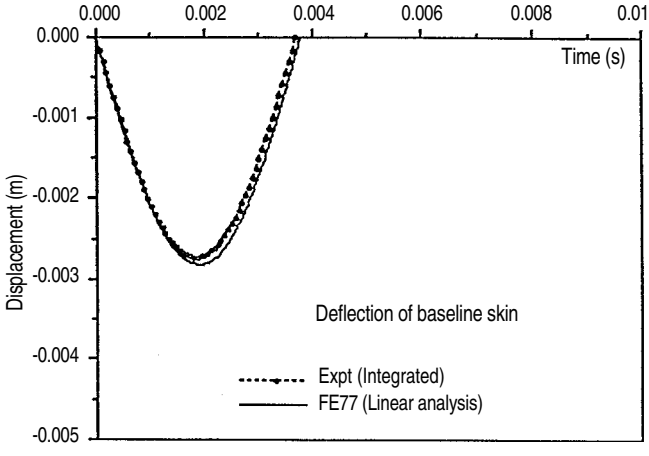

b) Deflection of impact point

Fig. 13 Comparison of FE prediction with test - low energy, small deflection
(Panel D, site M4, 6.4 J, without damage)

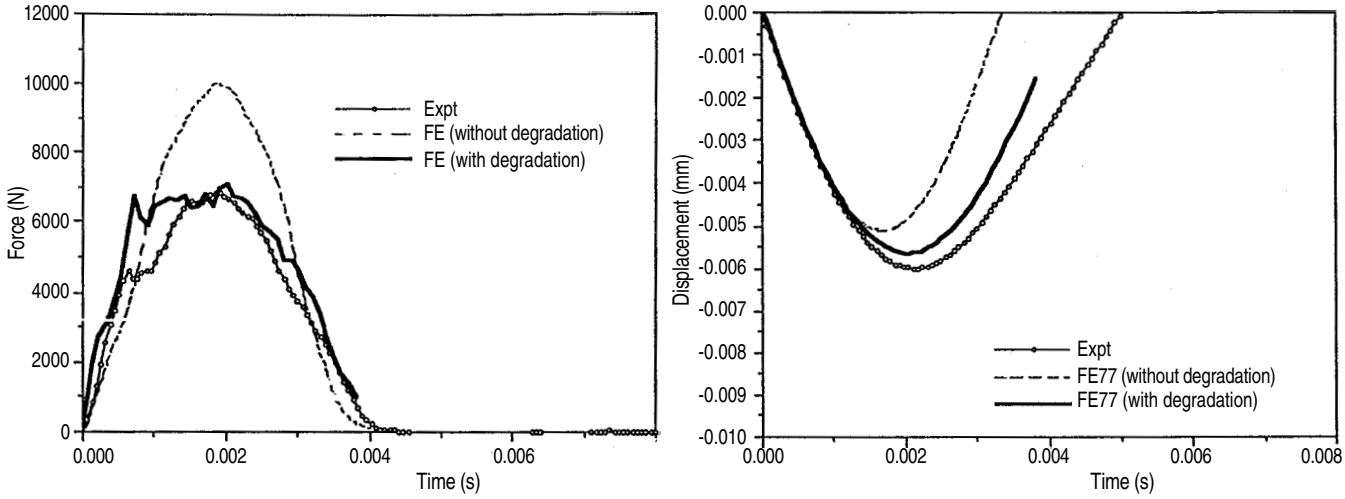

a) Impact force history

b) Deflection of impact point

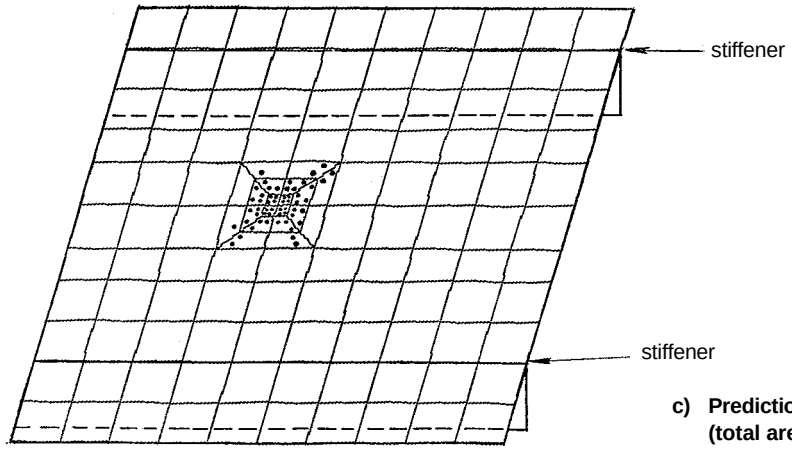

c) Prediction in-plane damage (total area = 1230 mm^2)

Fig. 14 Comparison of FE prediction with test - higher energy, large deflection (Panel C, site M3, 26 J, with damage)

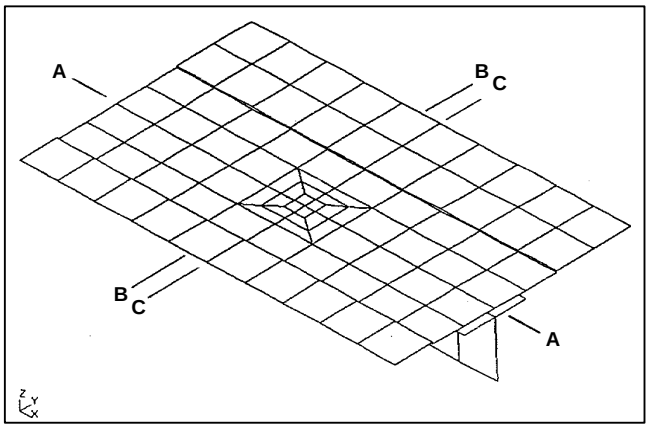

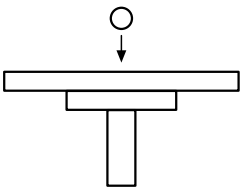

a) Local view of FE model near impact site over stiffener centre

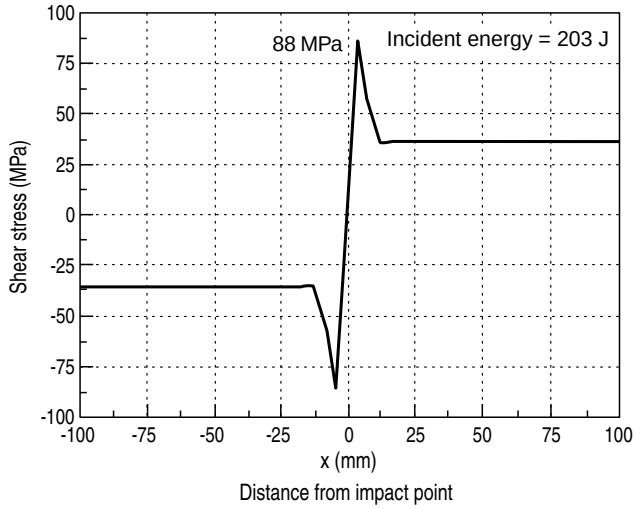

b) Flange transverse shear stress distribution along stiffener (line A-A)

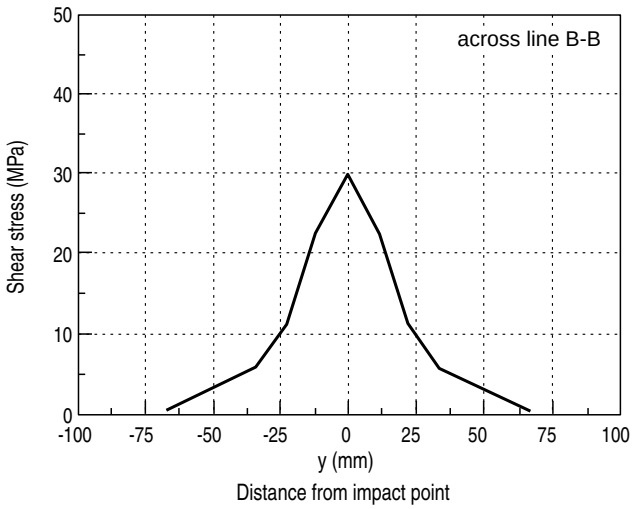

c) Transverse shear stress distribution across the stiffener flange (line B-B)

Fig. 15 Transverse shear stress distributions for impact over stiffener centre (Panel D, site S5, 203 J)

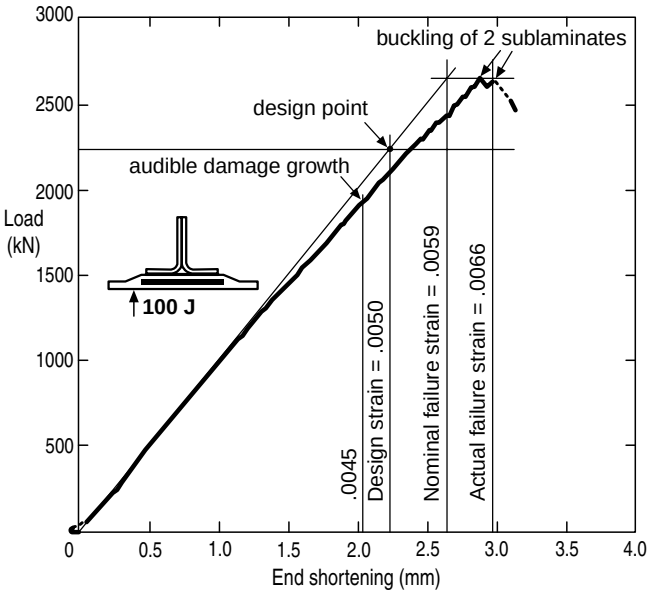

Fig. 16 Load versus end shortening of 3-stringer panel A with 100 J damage

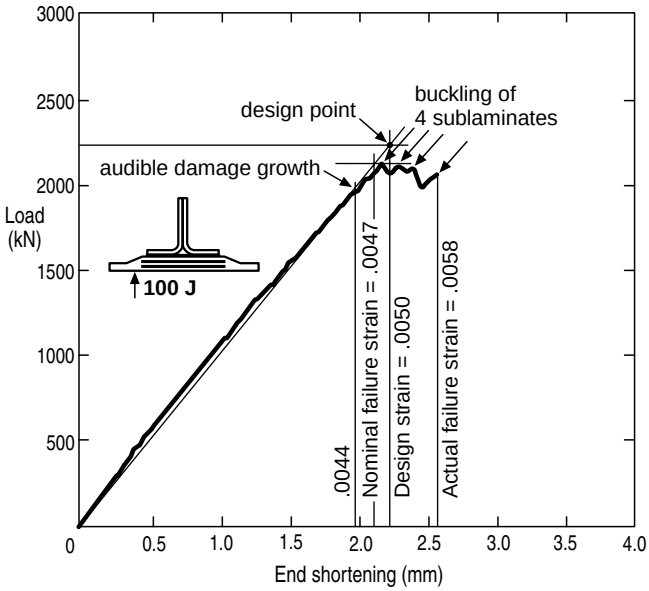

Fig. 17 Load versus end shortening of 3-stringer panel B with 100 J damage

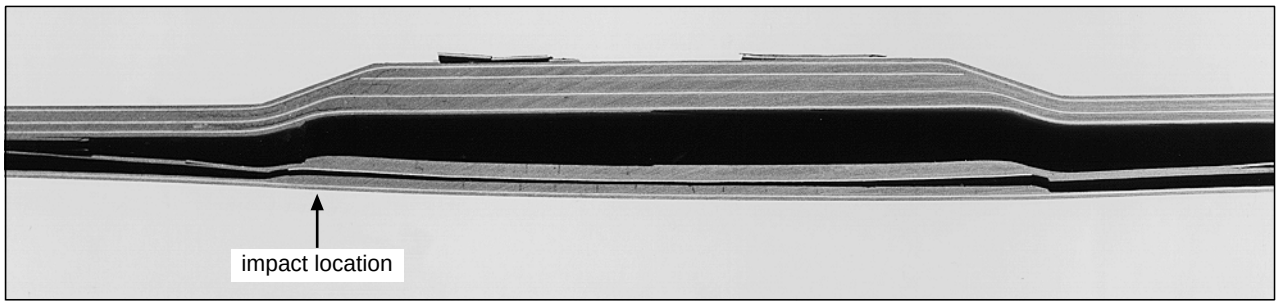

Fig. 18 Failure mode of panel A

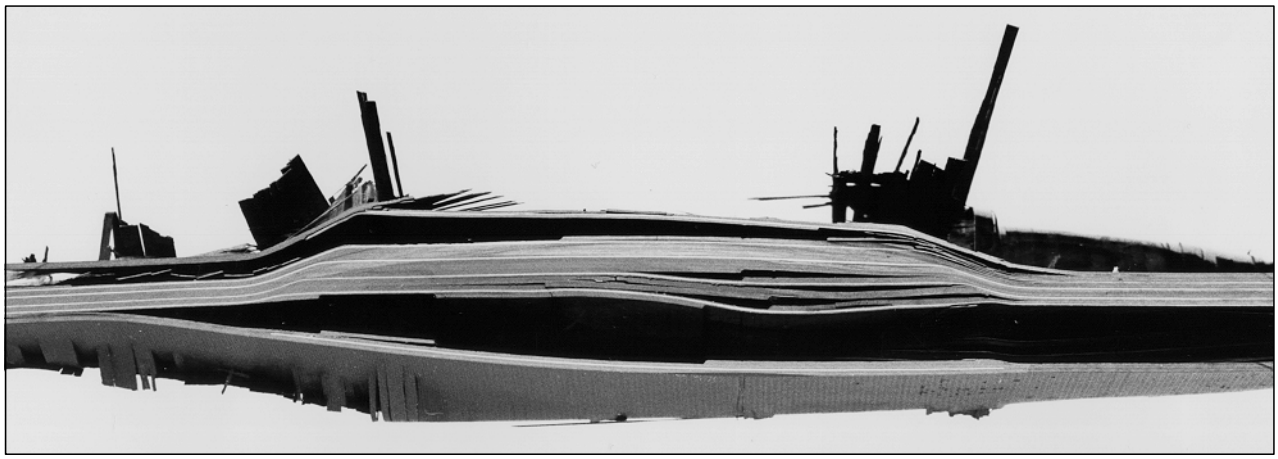

Fig. 19 Failure mode of panel B

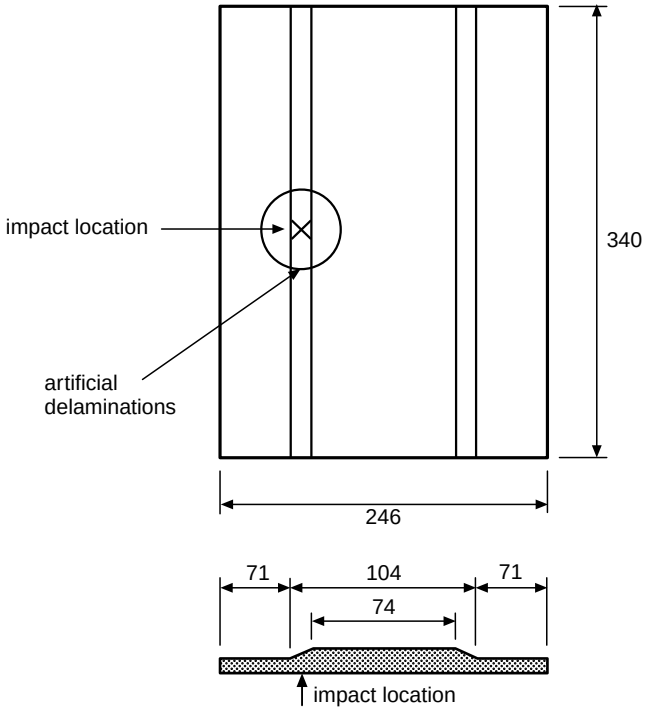

Fig. 20 SR-specimen geometry and location of impact and artificial delaminations

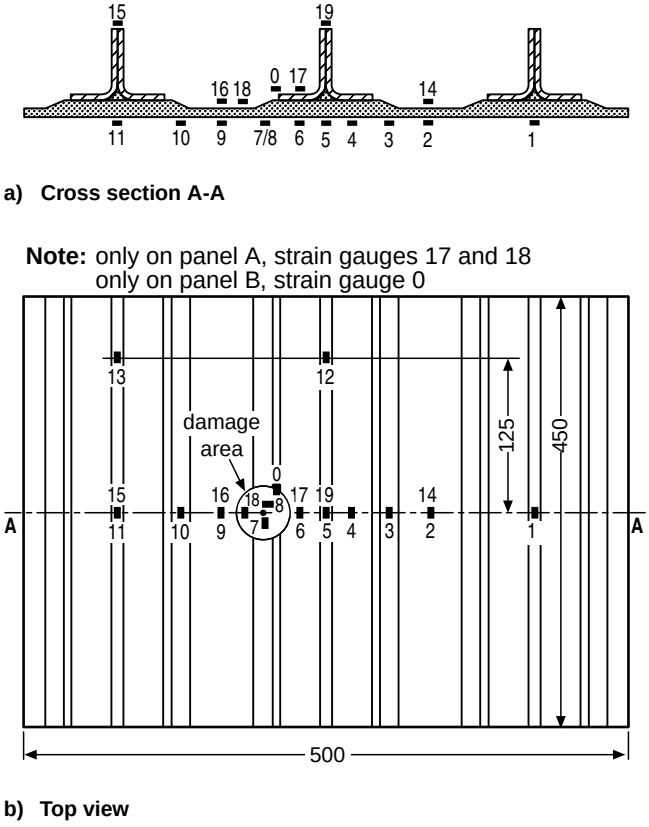

Fig. 22 Strain gauge positions on panels C and D

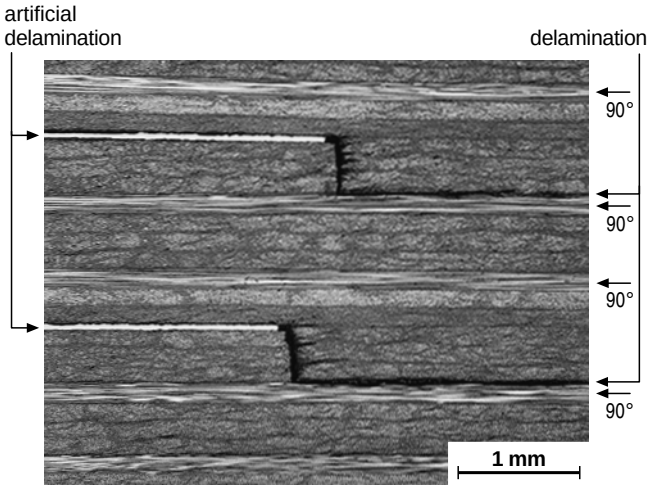

Fig. 21 Delamination growth from artificial delaminations towards 90-degree layers

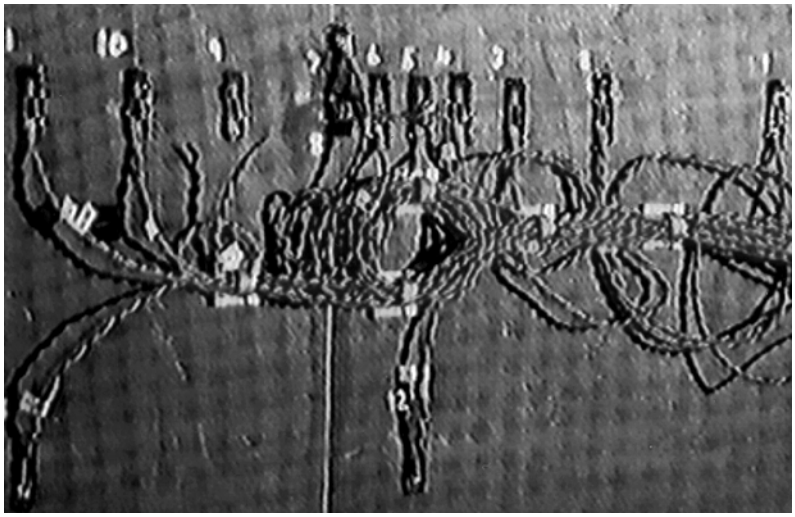

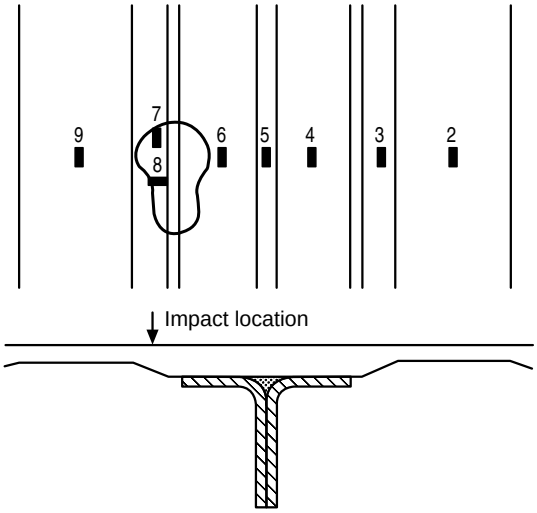

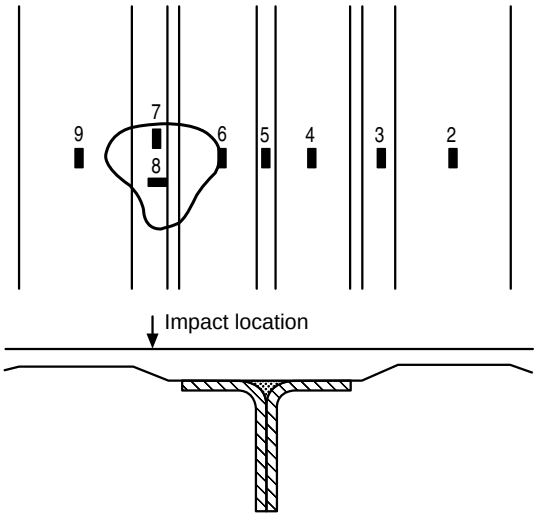

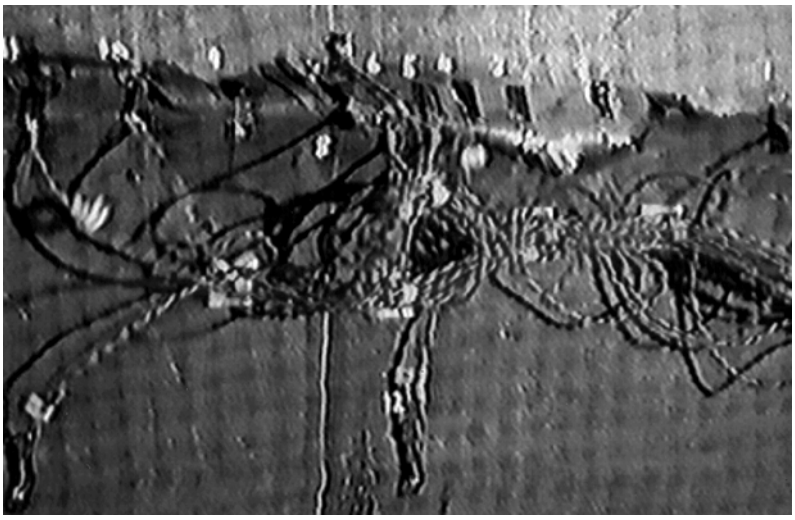

Fig. 23 Sublaminate buckling and collapse of panel C

Fig. 24 Non-symmetric deformation due to collapse of 0-degree ply stacks (Ref. 16)

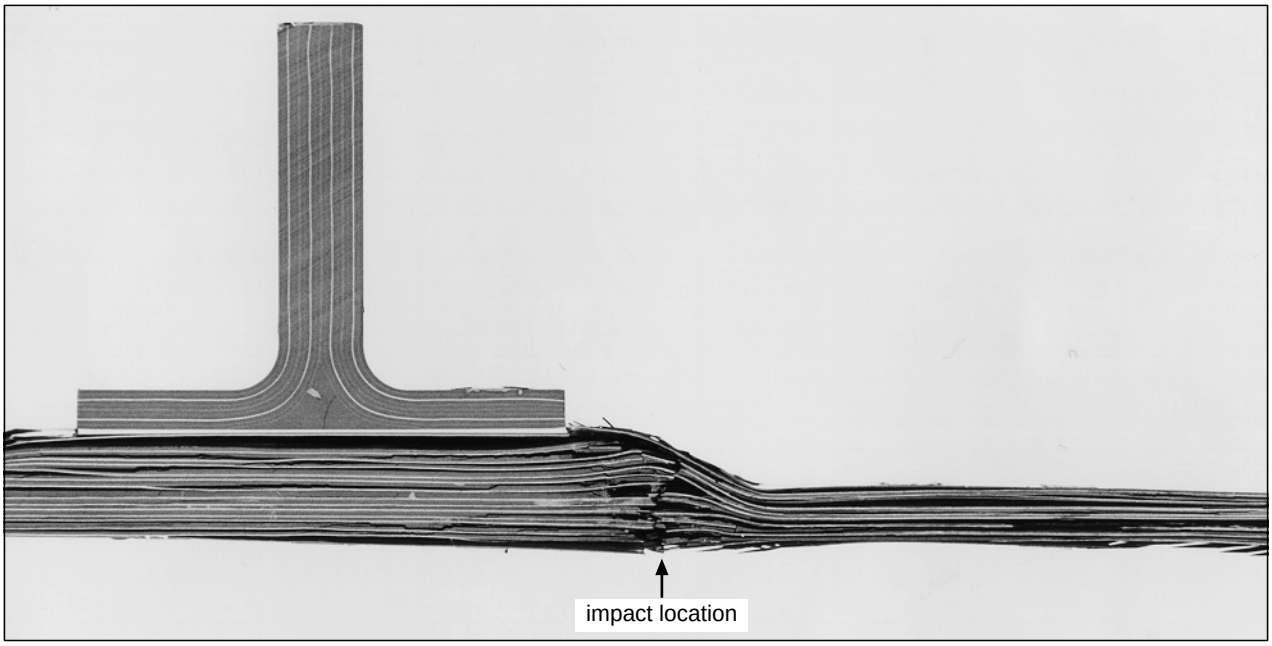

Fig. 25 Post-mortem view of panel C

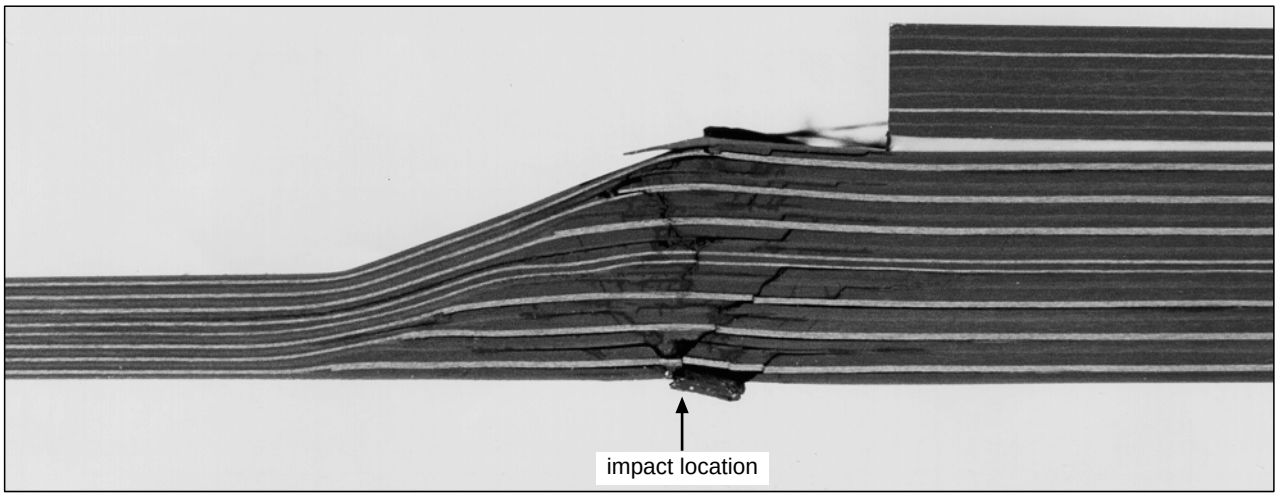

Fig. 26a Post-mortem view of panel D

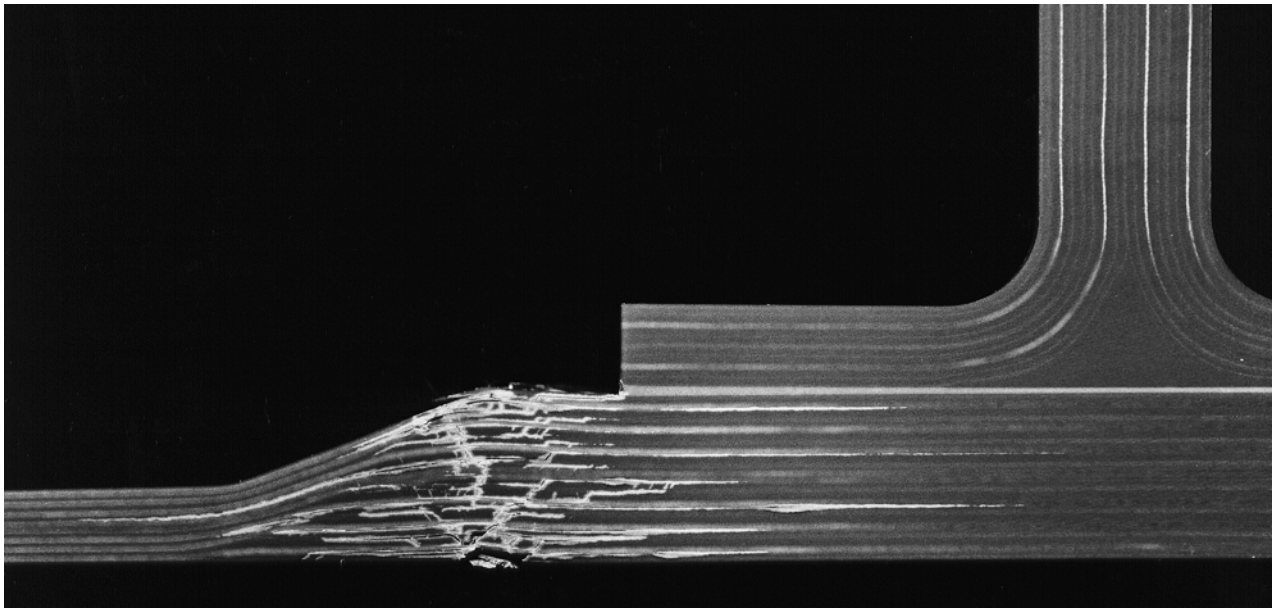

Fig. 26b Locations of major delaminations of panel D

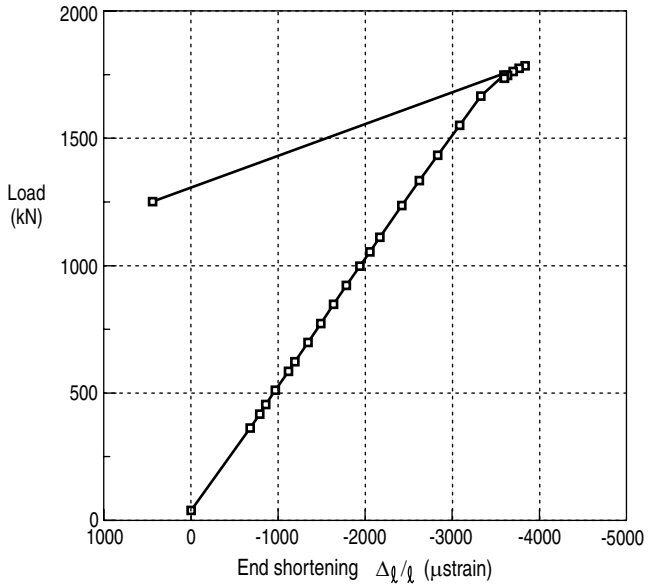

a) Load versus end-shortening curve of panel C, second test run

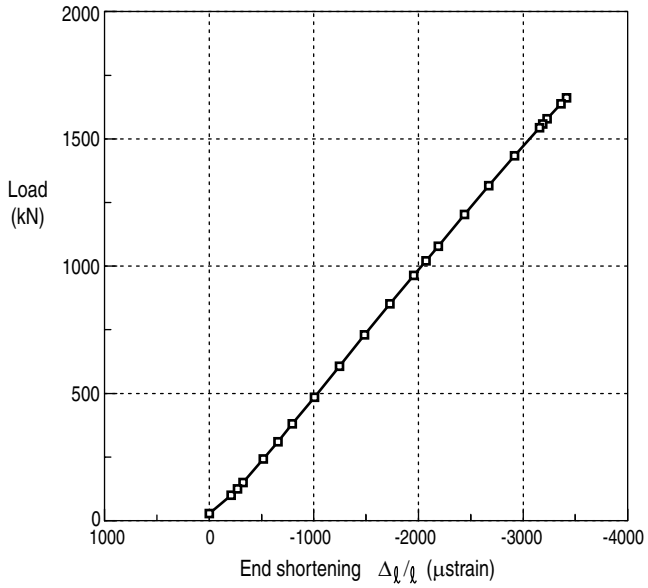

b) Load versus end-shortening curve of panel D, third test run

Fig. 27 Load versus end-shortening

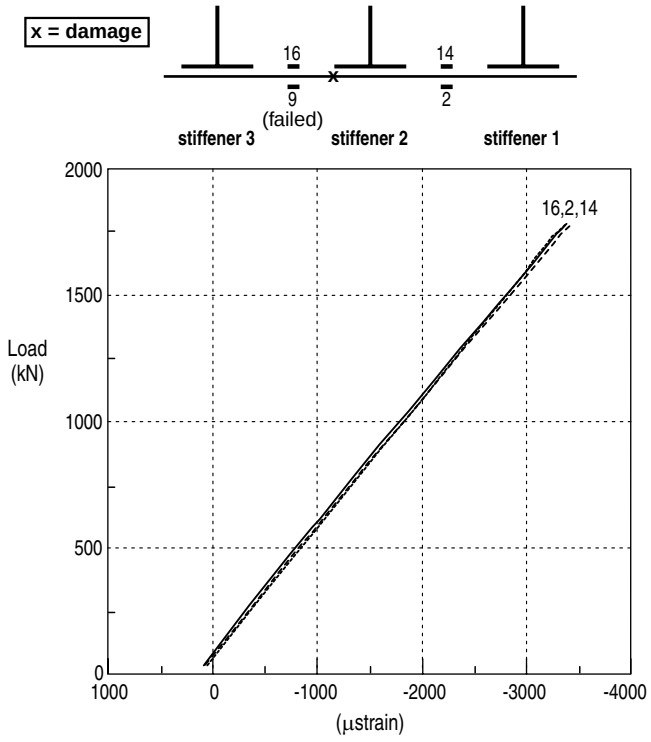

a) Skin bending of panel C recorded with strain gauges 2, 14 and 16

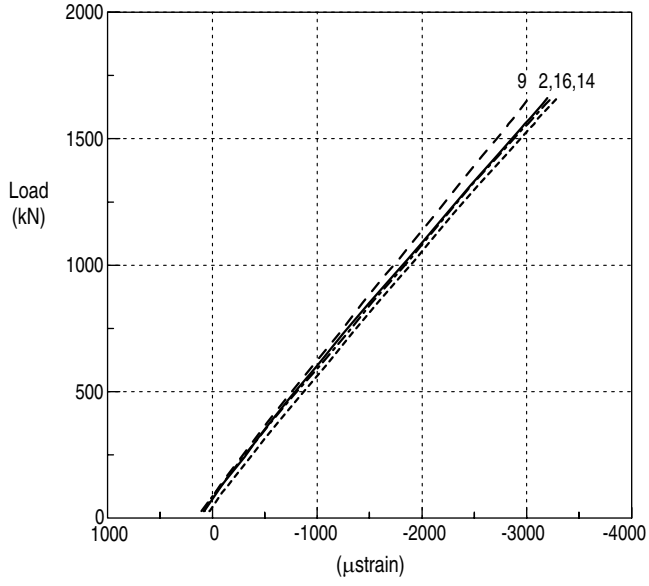

b) Skin bending of panel D recorded with strain gauges 2, 9, 14 and 16

Fig. 28 Skin bending

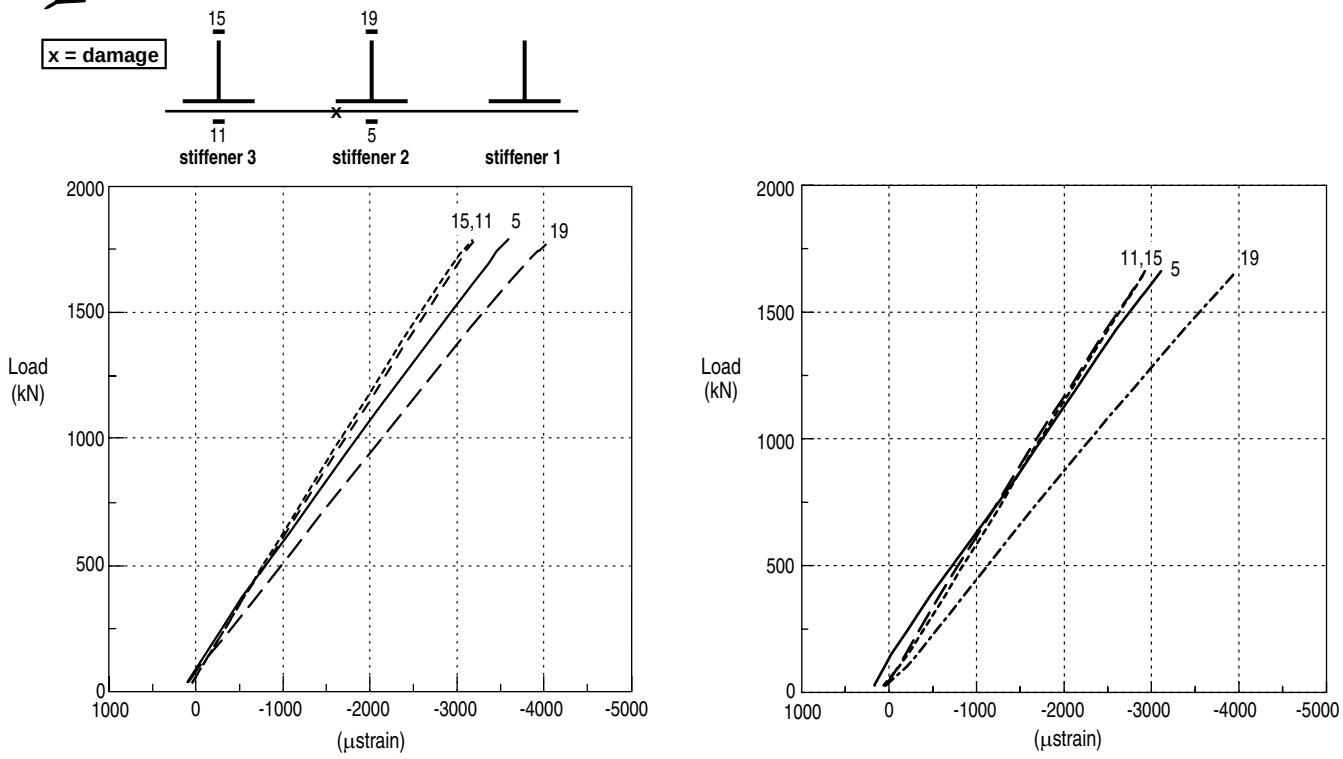

a) Stiffener bending of panel C recorded with strain gauges 5, 11, 14 and 16

b) Stiffener bending of panel D recorded with strain gauges 5, 11, 15 and 19

Fig. 29 Stiffener bending

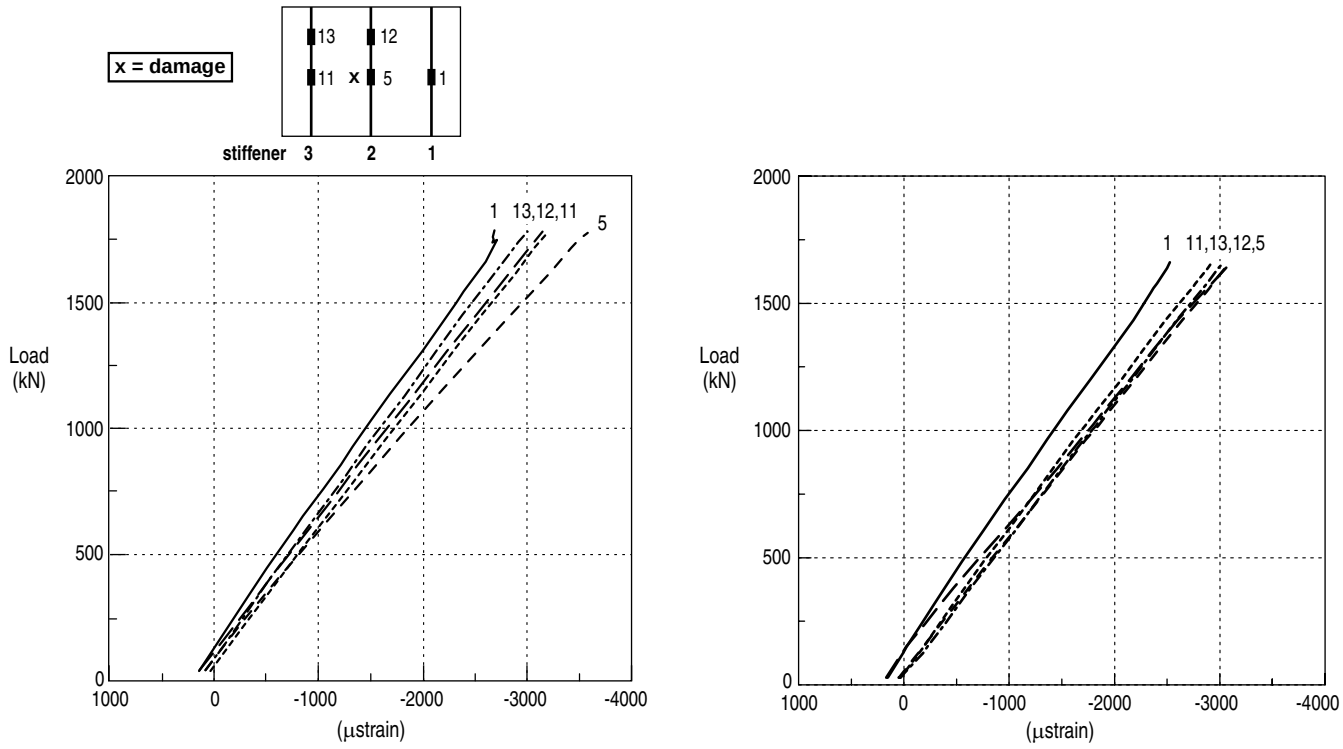

a) Strain distribution across panel C recorded with strain gauges 1, 5, 11, 12 and 13

b) Strain distribution across panel D recorded with strain gauges 1, 5, 11, 12 and 13

Fig. 30 Load redistribution

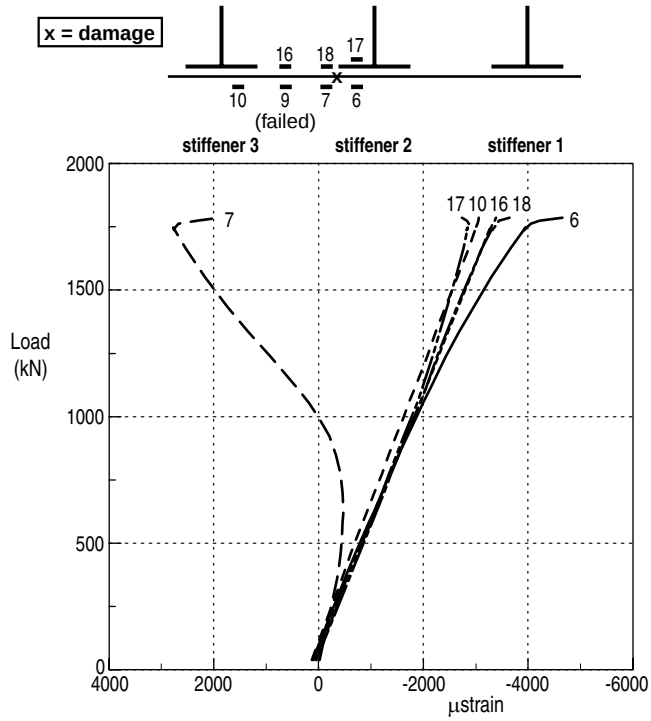

a) **Strain distribution across the damage site of panel C, recorded with strain gauges 6, 7, 10, 16, 17 and 18**

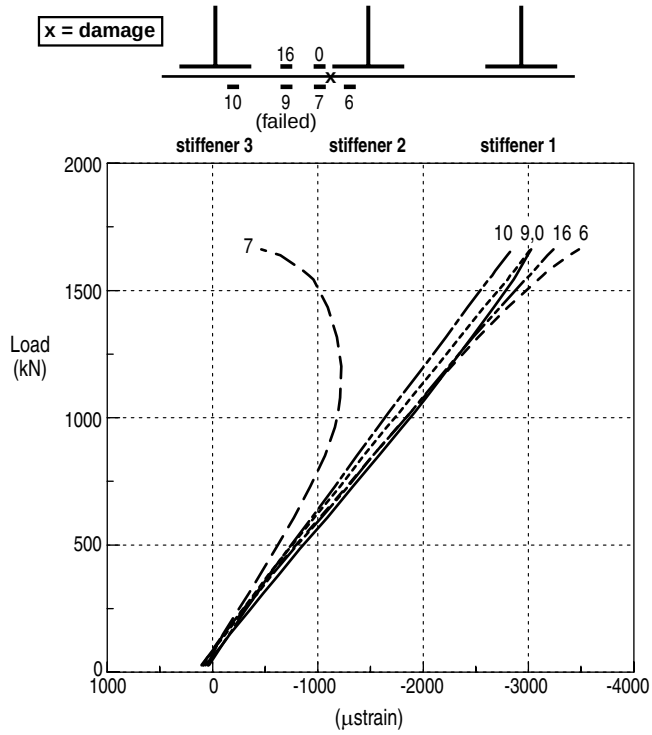

b) **Strain distribution across the damage site of panel D, recorded with strain gauges 6, 7, 10, 16, 17 and 18**

Fig. 31 Strain distribution

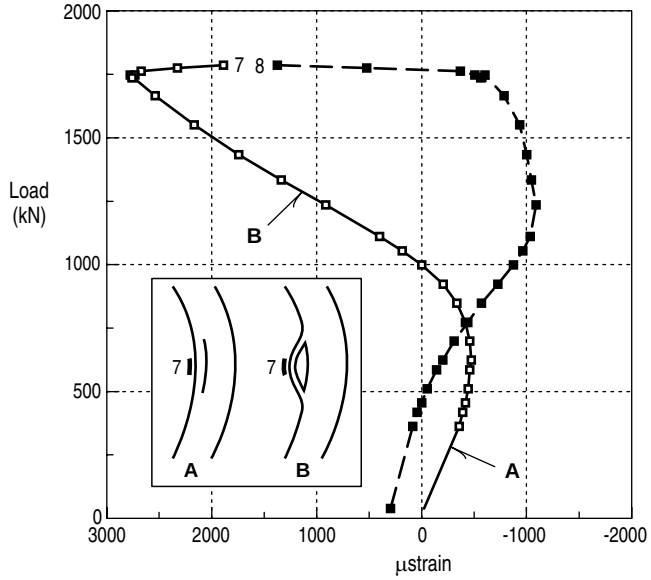

a) **Strains at the damage site of panel C, recorded with strain gauges 7 and 8**

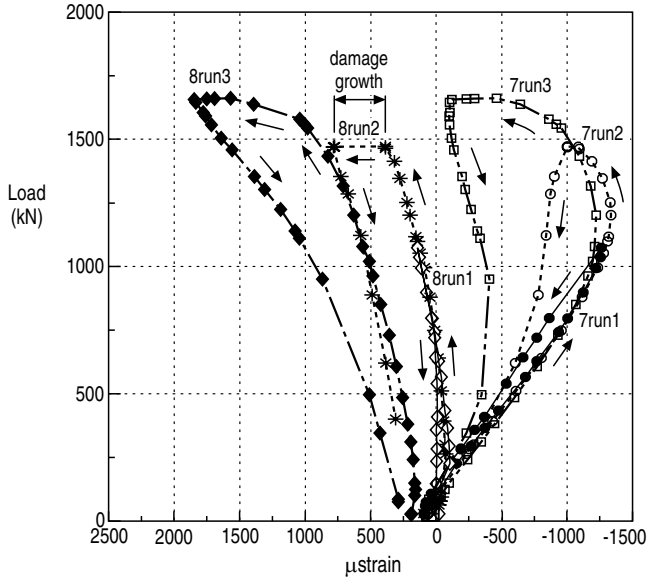

b) **Strains at the damage site of panel B, recorded with strain gauges 7 and 8**

Fig. 32 Strains at damage location